AFRL-AFOSR-UK-TR-2011-0031

Perching Experiment at Low Reynolds Number: Force and PIV Measurements of Rectangular Flat Wing Models in Perching Motion

Rolf E. Radespiel

Technische Universitat Braunschweig
Institute of Fluid Mechanics
Bienroder Weg 3
Braunschweig, Germany 38106

EOARD GRANT 10-3008

November 2010

Final Report for 01 November 2009 to 01 November 2010

Air Force Research Laboratory
Air Force Office of Scientific Research
European Office of Aerospace Research and Development
Unit 4515 Box 14, APO AE 09421

REPORT DOCUMENTATION PAGE

Form Approved OMB No. 0704-0188

1. REPORT DATE *(DD-MM-YYYY)*	2. REPORT TYPE	3. DATES COVERED *(From – To)*
10-11-2010	Final Report	1 November 2009 – 1 November 2010

4. TITLE AND SUBTITLE

Perching Experiment at Low Reynolds Number: Force and PIV Measurements of Rectangular Flat Wing Models in Perching Motion

5a. CONTRACT NUMBER

FA8655-10-1-3008

5b. GRANT NUMBER

Grant 10-3008

5c. PROGRAM ELEMENT NUMBER

6. AUTHOR(S)

Professor Rolf E. Radespiel

5d. PROJECT NUMBER

5d. TASK NUMBER

5e. WORK UNIT NUMBER

7. PERFORMING ORGANIZATION NAME(S) AND ADDRESS(ES)

Technische Universitat Braunschweig
Institute of Fluid Mechanics
Bienroder Weg 3
Braunschweig, Germany 38106

8. PERFORMING ORGANIZATION REPORT NUMBER

N/A

9. SPONSORING/MONITORING AGENCY NAME(S) AND ADDRESS(ES)

EOARD
Unit 4515 BOX 14
APO AE 09421

10. SPONSOR/MONITOR'S ACRONYM(S)

AFRL/AFOSR/RSW (EOARD)

11. SPONSOR/MONITOR'S REPORT NUMBER(S)

AFRL-AFOSR-UK-TR-2011-0031

12. DISTRIBUTION/AVAILABILITY STATEMENT

Approved for public release; distribution is unlimited. (approval given by local Public Affairs Office)

13. SUPPLEMENTARY NOTES

14. ABSTRACT

This report comprises aerodynamic measurements of a wing in perching motion carried out with the MAVlab facility at the Institute of Fluid Mechanics of Braunschweig University. In this context, the perching motion is modeled according to the wing motions of birds to rapidly reduce velocity when landing on a small spot i.e. a perch. The here discussed perching motion is defined as a discontinuous pitching of a wing from low starting angles of attack to high final angles. The study was carried out with two rectangular plan shaped flat plate wings performing the perching motion from 0° to 45° angle of attack. Force measurements with an internal balance were taken for combinations of Reynolds numbers and reduced frequencies. 2D-particle-image-velocimetry of the flow field was carried out for different time stages of one particular combination, where the force measurements indicate changes in the flow field to occur, to understand the complex unsteady aerodynamic response to this motion type.

15. SUBJECT TERMS

EOARD, Aerodyanamics, Wind Tunnel Testing, Micro Air Vehicle

16. SECURITY CLASSIFICATION OF:			17. LIMITATION OF ABSTRACT	18, NUMBER OF PAGES	19a. NAME OF RESPONSIBLE PERSON
a. REPORT	b. ABSTRACT	c. THIS PAGE			Gregg Abate
UNCLAS	UNCLAS	UNCLAS	SAR	73	19b. TELEPHONE NUMBER *(Include area code)* +44 (0)1895 616021

EOARD: FA8655-10-1-3008

REPORT ISM-2010/3 with addendum

Perching Experiment at Low Reynolds Number:
Force and PIV Measurements of Rectangular Flat Wing Models in Perching Motion

R. Wokoeck

Institute of Fluid Mechanics
Technische Universität Braunschweig
Bienroder Weg 3
38106 Braunschweig

Braunschweig, 10th of November 2010

This report contains:

58 Pages
38 Figures
6 Tables
1 Data Storage Device
1 Addendum

Table of contents

1 Introduction

This report comprises aerodynamic measurements of a wing in perching motion carried out with the *MAVlab* facility at the Institute of Fluid Mechanics of Braunschweig University.
In this context, the perching motion is modelled according to the wing motions of birds to rapidly reduce velocity when landing on a small spot i.e. a perch. The here discussed perching motion is defined as a discontinuous pitching of a wing from low starting angles of attack to high final angles. The study was carried out with two rectangular plan shaped flat plate wings performing the perching motion from 0° to 45° angle of attack. Force measurements with an internal balance were taken for combinations of Reynolds numbers and reduced frequencies. 2D-particle-image-velocimetry of the flow field was carried out for different time stages of one particular combination, where the force measurements indicate changes in the flow field to occur, to understand the complex unsteady aerodynamic response to this motion type.

2 General set up and specimen

2.1 MAVlab Facility

The *MAVlab* facility was designed to investigate low Reynolds number unsteady aerodynamics of MAV size 3D-specimen. It consists of three key components: The LNB windtunnel, a model support to perform high dynamic motions and a very small 6 components internal balance (see chapter 6.1).

LNB Windtunnel

The LNB windtunnel (figure 1) is a continuous Eiffel type tunnel with room recirculation that runs at velocities from 4 to 19m/s. It offers closed, modular test sections 1500mm long, 400mm wide and 600mm high. The tunnel is driven by a 9 bladed fan in suction mode powered by a 3000W motor. The proportional plus integral type control loop for the tunnel velocity is realized via a software that also monitors room pressure, temperature and humidity. The wind tunnel is designed to meet the requirements of investigations at low Reynolds numbers for studies of MAVs, 2D-flapping wings and boundary layers. Various efforts (straightening and contraction, several means of vibration and sound damping etc.) are implemented to achieve a high quality flow with low turbulence and perturbation. The flow in the test section is characterized by a typical turbulence level of Tu<0.1% at 10m/s and a core velocity uniformity of 99%.

Dynamic 3D model support

The dynamic model support (figure 2) is built into one of the modular test sections. It was designed for moving small 3D specimen with precise 3 degrees of freedom in the upright centre plane with high velocity and acceleration. The drives are of linear direct type, which was found to be the only design type that is capable of delivering the necessary acceleration forces whilst offering the required accuracy to meet the design targets of the support. Each of the drives delivers a maximum of 700N consuming 1950 W. The drives are controlled in a real-time closed loop with a 12bit virtual cam resolution plus smooth interpolation and on the fly correction up to an allowed level of misalignment before emergency halt.
The design targets of the model support related to accuracy are the two standard motions

- harmonic plunging with ±150mm amplitude @ 3Hz and
- harmonic pitching with ±20° amplitude @ 3Hz,

for which the repetitive accuracy of ±0.05mm respectively ±0.1° is assumed. A high precision measurement of the actual motion accuracy is scheduled for late 2010 via Image Pattern Correlation Technique.
The actual stage of completion features only two of the three drives needed for a complete decoupling of all 3 degrees of freedom. Whilst pure plunging motions are carried out precisely, any motion containing a rotative portion is accompanied by a small horizontal translation, which the third drive was planned to compensate for. This unwanted translation has a stroke amplitude proportional to $1-\cos\hat{\alpha}$ and thus may be neglected for motions with small pitch amplitude $\hat{\alpha}$ or – like in the studied perching cases – with relatively low reduced frequencies k, where k for this rotational but discontinuous motion is defined as follows:

$$k = \frac{1}{2}\frac{\text{chord}}{U_\infty}\frac{\partial \alpha}{\partial t} \tag{2.1}$$

2.2 Wind Tunnel Models

Wing Models

Figure 3 shows the models utilized for this study. Their geometries differ only in span. Except for the tubular fuselage, which houses the balance, the models are flat plates with rectangular plan shapes, a thickness of 2.7mm and fully rounded edges and corners. The chord is 117mm and the span of the smaller model called *AR2* (aspect ratio 2) is 234mm resulting in 27378mm^2 wing area. The larger model, called *ARinf*, was designed to work as if aspect ratio was infinite by spanning almost from one side of the test section to the other. Since the model is moving relatively to the section walls, the wingtips are located at 4mm distance from the walls, which is far inside the wall boundary layers, so that a strong blocking effect acting against the flow around the wingtips can be expected. The span of the *ARinf* model is 371mm resulting in 43407mm^2 wing area. Both models are designed to be stiff so that deformation due to the effective forces may be neglected and at the same time light (65g for *AR2* and 91g for *ARinf*), to keep the inertial forces compared to the aerodynamic forces as low as possible. Therefore, a sandwich design was chosen with two layers of reinforced carbon fibre on the upper and lower wing surface and a 2mm thick foam plate and a wooden skeleton structure in between. The two carbon layers are linen fibre cloth with 0° and 90° fibre direction on the inner layers and +45° and -45° fibre direction on the outer layers in respect to the fuselage centre axis. The wing edges are made of round carbon fibre sticks that connect the carbon fibre surfaces together and thereby stiffening the wing structure as a whole. The wooden skeleton inside the wings helps directing all effective forces from the wings into the aluminium fuselage nose that acts as the balance fastener, through which all forces are directed into the balance. The rest of the fuselage, located exactly in the middle, is made of a 1mm strong carbon fibre plastic pipe and connects the two wings.

Inertial Force Dummies

With the used setup the aerodynamic forces, which are subject of the measurements, are recorded together with the inertial forces caused by the mass of the model and the balance when in accelerated motion. Previous measurements have shown that the inertial forces for the investigated motions are of the same magnitude as the aerodynamic ones. For the necessary separation a second measurement without the aerodynamic forces (windtunnel not running) is done to later determine the aerodynamic forces by subtraction between both measurements. It is obvious that the above prescribed method does not account for the inevitable aerodynamic interaction caused by the specimen when moved through motionless air. The amount of this unwanted forces is directly related to the wing area and motion velocity and will add substantial damping to the second measurement represented by a hysteresis in the measurement plots. Such hysteresis in the answer to inertial forces cannot be accepted. As a solution to this problem, the second measurement is performed not with the model but with a dummy mounted. The dummy has the same mass, centre of mass and most important inertial moment in reference to the pitching axis as the model, but interacts much less with the surrounding air due to its small shape.

Figure 4 shows the inertial force dummies of the *AR2* and *ARinf* models. The first was developed during previous measurements with the *AR2* model which had proven this methology of force separation to be sufficient and robust. The second is a new, more universal design that features the same fuselage as all the produced flat plate models and can be fitted with different slide on masses representing the mass distribution of different models.
The production of the *ARinf* model and the modular dummy was part of this measurement campaign. The fine-tuning on the dummy to deliver the same inertial moment was carried out. The moments of the model and its dummy were measured indirectly by determination of the time period with the model or dummy swinging in the pitching plane. The setup shown in figure 5 uses a spring as energy storage, a light barrier as trigger and a *Tektronix 3431L* oscilloscope for the time measurement. The iterative fine-tuning of the slide on mass was conducted until the difference between the dummy and the model period was -0.0195s or -0.71% resulting in a difference in the inertial moment of -2.82%. The measurements taken in the final iteration are listed in Table 1. The fact that the remaining difference between model and dummy is close to the standard deviations shows that the maximum precision to be gained with this setup was reached.

		model period [s]	**dummy period** [s]
measurement point 1		2.7700	2.7650
measurement point 2		2.7700	2.7450
measurement point 3		2.7650	2.7400
measurement point 4		2.7550	2.7200
measurement point 5		2.7800	2.7600
measurement point 6		2.7650	2.7500
measurement point 7		2.7550	2.7500
measurement point 8		2.7650	2.7250
measurement point 1		2.7650	2.7550
measurement point 10		2.7500	2.7350

average value	[s]	2.7640	2.7445
standard deviation	[s]	0.0088	0.0146
difference dummy to model	[s]		-0.0195
difference dummy to model	[%]		-0.71

Table 1: Values of the final fine-tuning step for the *ARinf* Dummy:

3 Modifications

3.1 Refitting of the Test Section

In case of a complete failure of all implemented security systems of the motion apparatus, it is foreseen to let the models punch through destructible ceiling and floor areas of the test section. These destructible areas are made of aluminium foil, which due to the adverse effect of impact velocity on the ductility of metals will tear apart with relatively low forces that the balance can cope with. Since the *ARinf* model has a larger span than taken into account during the design phase of the test section, the wingtips would in such an event hit rigid structures around and below the aluminium foil areas in the floor. To avoid this, the test section is refitted with new sidewalls which are seated on top of the mentioned rigid structures, effectively narrowing the cross area of the test section from 400mm width down to 379mm width. The two acrylic walls can be slid back and forth to give access to the inside. This modification is intended to be not permanent and will be reset after the measurement campaign is finished.

3.2 Refitting of the Sting

To change the α range from the standard pitching [-20°; +20°] to the [0°; +45°] perching, a new sting had to be manufactured. Near the model, the new sting features a 45/2° elbow for the asymmetric range. It is also shorter, to make full use of the maximum strokes of the drives. The new sting was built out of an existing one. It is shown in figure 6 together with the chopped off head to demonstrate the reduction of the overall length. In the vicinity of the elbow, the balance cable is routed outside the sting to maintain sufficient stability and stiffness of the sting without increasing its diameter, which is limited by the translative bearing size placed on the first of the two pushrods.

4 Motion Definition

4.1 Perching Motion

As explained above, the perching motion in this work is defined as a ramp function of the angle of attack over time. The simplest of such ramps has a constant pitching velocity $\dot{\alpha} = \text{const.}$ in its middle section (see figure 7). It can be defined as follows:

$$\alpha_{(t)} = \begin{cases} \alpha_0 & ; \quad t_0 \le t < t_{start} \\ \dot{\alpha}\, t & ; \quad t_{start} \le t \le t_{stop} \\ 2\hat{\alpha} & ; \quad t_{stop} < t \le t_\Omega \end{cases} \quad \text{with} \quad t_{move} = t_{stop} - t_{start} \quad \text{and} \quad t_{wait} = (t_\Omega - t_0) - t_{move} \tag{4.1}$$

Such an idealized function is not continuously differentiable twice, which means it implies infinite accelerations $\ddot{\alpha}$ at the beginning and end of the motion. The motion function to be carried out in real applications has to have sections of acceleration at the beginning and end of the motion. Opposing interests can be formulated:

i. One goal of optimization is to keep those acceleration sections short relative to the section of constant pitching velocity to stay close to the ideal shape.

ii. Another goal is to gain a high pitching velocity to realise high reduced frequencies *k*, since the dynamic effects are of interest to this study.

No mechanic system under dynamic load is free of vibrations. The combined causes for vibration in this system are:

- dynamic effects in the control loop,
- the design of the linear drives (the distance between the magnets etc.),
- masses, sizes and stiffness of the moving parts defining their eigenfrequencies and deformations,
- tolerances, clearances and slip-stick effects in the joints of the parts,
- etc.

Both, the achievable pitching velocity $\dot{\alpha}$ and the pitching acceleration $\ddot{\alpha}$ are limited by the performance of the drives and increasing them raises the level of vibrations. It is also necessary to define a motion function that is continuously differentiable more than twice to avoid jolts, which impair the force measurements substantially and also cause vibrations. Thus,

iii. one more goal of optimization is to keep forces of acceleration and higher derivatives low to avoid a high vibration level and to maintain a good ratio between the aerodynamic and the inertial forces in the balance signals.

It is possible to gain such a function by the principle of harmonics composition, which is the standard method for signal generation in electronics and telecommunication engineering for example. The finally programmed function of α over time for this study was defined as follows:

$$\alpha_{(t)} = \alpha_0 + 2\hat{\alpha}\ln\left(\frac{\cosh(A(t-t_1))\cdot\cosh(A(t-t_4))}{\cosh(A(t-t_2))\cdot\cosh(A(t-t_3))}\right) \quad with$$

$$A = a\frac{U_\infty}{chord} \quad and \tag{4.2}$$

$$t_1 = t_0 + \frac{1}{2}t_{wait};\quad t_2 = t_0 + \frac{1}{2}t_{wait} + t_{move};\quad t_3 = t_0 + \frac{3}{2}t_{wait} + t_{move};\quad t_4 = t_0 + \frac{3}{2}t_{wait} + 2t_{move}$$

Function 4.2 (also plotted in figure 7) prescribes the perching motion in the first half and then its exact reverse, returning to α_o. This behaviour is welcomed, as it is also a necessity for the periodic execution by the apparatus. The time domain $[t_0; 2t_\Omega]$ in which equation 4.2 can be used for this purpose represents one period, which is:

$$P = 2t_{wait} + 2t_{move} = 2(t_\Omega - t_0) \tag{4.3}$$

t_{wait} was chosen to be three times t_{move}, to assure that before each perching motion execution, the history of the previous back travel in the flow field has been converged and to assure that after the end of the perching motion, the measurement can continue until the quasi-static status is reached.
It has to be mentioned that function 4.2 actually has no linear sections at all. To compare this function to the ideal one, here the following terminology is prescribed:

> *Those parts of function 4.2, where the local $\dot{\alpha}$-value differs more than 1% from zero or more than 1% from the maximum pitching velocity $\dot{\alpha}_{max}$, which can be found at $\alpha = \alpha_o + \hat{\alpha}$ (half pitch stroke), are referred to as **"acceleration sections**".*
> *The others are referred to as "**linear sections**", amongst which those with $\dot{\alpha}$ near zero are called "**motionless**" whilst the sections with $\dot{\alpha}$ close to $\dot{\alpha}_{max}$ are called "**constant speed**".*

In Equation 4.2, parameter *a* is a shape factor for the accelerated sections. The higher *a* is, the sharper are the corners of the α-slope and thus the larger are the acceleration values but also the smaller are the accelerative sections compared to the section with constant speed. For $a \mapsto \infty$ the first half of equation. 4.2 will meet equation. 4.1.

Tests with combinations of $\dot{\alpha}$ and *a* were carried out and revealed, that appearing vibrations (which were measured in emitted sound levels) within the apparatus grow proportional to both parameters so that a useful operational limit was derived (see figure 8). A working point for the experiment at a secure distance to this limit was defined for a perching from α=0° to 45°. The value of $a = 0.88$ results in a motion path with a constant speed section, that stretches 60% of the full pitch stroke ($2\hat{\alpha}$). Consequently, the other 40% are divided equally into the prior 20% of acceleration and the following 20% of deceleration.

4.2 Programming Procedure

The programming procedure comprises the following steps, where the fine-tuning is carried out as an iterative loop inside:

1. Calculation of the pitching motion of the specimen following equation 4.2 via *Microsoft Excel* resulting in discrete coordinates with both the number of coordinate points and the number of decimal places much higher than the controller of the drive is capable of, to avoid errors of discretisation in the following process steps. The period

comprehends thus two pauses t_{wait} and two motions t_{move}, each directly comparable to the sections of the ideal ramp function. The pause t_{wait} prior to the perching move is necessary to reach the quasi-static state before each of the consecutive measurements. As a further step, the number of decimal places is reduced until any reverse in motion stemming from the harmonic composition disappears. The so defined coordinate set is normalized to a period of 1s for the next programming steps. The excel file is attached to the report.

2. The conversion of the specimen movement into the movement of the drives is carried out with a virtual representation of the model support by the COSMOS-motion simulation package of the CAD software system SolidWorks (Version 2006SP4.1). The coordinate set of step 1 is fed into the software for the motion path definition of the specimen together with a smooth spline interpolation. The motion paths of the drives (called virtual cams) are exported into the .csv file format. Here, a resolution of 4096 coordinate points is used, which is the maximum capacity of the controller.

3. The virtual drive cams are being processed via the program *converter*, which was written at ISM. It is capable of a) a linear stretching of the cam in space and time and b) adding an effective time shift to the cam using spline interpolation. The stretching in both dimensions is used for fine-tuning, when the amplification values offered by the controller are considered too coarse. The stretching in amplitude is used also as a first order correction of the shrink of amplitude effect, that occurs when the drives are lagging behind. This position lag of the drives is proportional to their velocity and is an inevitable part of any motion control system that only reacts instead to plan ahead. The time shift option is used to correct a very small time lag in between the two drives which was found to occur although the drive manufacturer claims that the orders for each drive are given and executed at exactly the same time.

4. The post processed cam files are converted into the proprietary format of the controller via the software *proCAM2* from *Baumüller Nürnberg GmbH*. , which is the producer of the drives and controller.

5. The controller is fed with the virtual cams via the software *ProProg WTII* from *Baumüller*.

6. The programmed motion is run and measured. The amplification values for speed (period *P*) and stroke amplitude are adjusted. The remaining deviation in amplitude and speed of both drives and the phase lag of the second drive are measured and used to start the iterative correction loop back at step 3, which is carried out until satisfactory values are found. In the present case, where new geometries (sting) are introduced with manufacturing tolerances, the dimensions of the new parts in the CAD simulation also have to be corrected and the iteration loop for this correction starts at step 2. As validation quantities for the second correction, the position and motion path of the rotational centre of the specimen were utilized.

4.3 Motion Accuracy by Prior Testing

Preparative tests for the measurement campaign were carried out with different perching motions, one having very similar parameters to the final chosen case I:

- $\alpha_0 = 0°; \quad 2\hat{\alpha} = 45°$
- a=0.785, thus 55% of the pitch stroke is better than 99% linear
- $\dot{\alpha}_{\max} = 203.8° / s$

The angle of attack plot over time (based on the drive position recordings) is shown in figure 9. It can be seen that α is superimposed by some waviness with an amplitude of about $\pm 0.0225°$ and a main frequency of around 50Hz, the causes for which were mentioned in chapter 4.1. It has to be pointed out, that these values were measured with no specimen mounted on the sting. The motion accuracy under the measurement conditions is discussed in chapter 8.

5 Measurement Cases

Table 2 holds all measurement cases and their varied motion parameters that were investigated during this campaign. t_{move} and t_{wait} can alternatively be expressed as *convective* times by the number of chord lengths, that a fluid element travelling with U_∞ would have passed during. Note that all cases are based on the one normalised motion function with a=0.88 as defined in chapter 4 and that only the velocity of the windtunnel and $\dot{\alpha}$ respective P have to be adjusted.

case	Re^*	U_∞	k	$\dot{\alpha}$	P	t_{move}	t_{wait}	meas. type
		[m/s]		[°/s]	[s]	[chords]	[chords]	
I	50000	6.47	0.030	190.23	1.8924	13.090	39.270	Force and PIV
II	50000	6.47	0.015	95.12	3.7848	26.180	78.540	Force
III	20000	2.59	0.030	76.09	4.7311	13.090	39.270	Force
IV	100000	12.95	0.015	190.23	1.8924	26.180	78.540	Force

Table 2: Motion variation within the measurement cases.
*(calculated with a kinematic viscosity of 1.515E-08m^2/s for air)

6 Force Measurements

6.1 Measurement Setup

The used balance W637 is one of the smallest 6 components balances available. It was tailored for the measurement of force derivatives of Micro Areal Vehicles on the dynamic model support of the *MAVlab*. Its dimensions are 107mm length, 11.2mm diameter and a mass of 35g. The working principle is a 3D bending beam with several strain gauges applied to it. The measurement range is

F_x: ±7N, M_x: ±0,750Nm,
F_y: ±20N, M_y: ±0,750Nm,
F_z: ±20N, M_z: ±0,374Nm,

with the x-axis pointing to the front, the y-axis pointing to starboard and the z-axis pointing downwards.
The voltages of the six electric bridges together with the position signals of the drives (coming from the controller) are processed and recorded with a time resolution up to 2400Hz with an *MGCplus* measurement system of *Hottinger Baldwin Messtechnik*. Together with this system, an accuracy of better than 0.0015% of the full scale values is achieved. Table 3 holds the settings used during the measurement.

case	*MGCplus filter frequency* [Hz]	*MGCplus sampling frequency* [Hz]	*number of recorded samples per event*	*number of recorded periods per event*	*number of recorded events per ensemble*
I	200	600	2400	2.11	50
II	200	300	2400	2.11	50
III	200	300	3000	2.11	50
IV	200	600	2400	2.11	50

Table 3: Measurement settings

6.2 Data Processing

The data of the balance measurement together with the wind tunnel data and the drive positions are processed in a hardware step followed by two steps in software. The processing inside the *MGCplus* hardware consist of amplification, low pass Bessel filtering with 200Hz (highest possible value), and 16 bit digitizing.
The signals are then handed over to the measurement software, which converts the 6 balance signals into the 3 forces and 3 moments. The measurement software stores the raw balance signals, the forces and moments, the drive positions and the wind tunnel values handed over from the wind tunnel control program.
Further processing is done with the a second program, which

- calculates the specimen position and inclination from the drive positions,
- separates the inertial forces from the aerodynamic forces with the methology prescribed in chapter 2.2
- translates the forces and moments from the balance coordinate system into the aerodynamic system,
- calculates the aerodynamic coefficients by the formula

$$c_i = \frac{X_i}{q_\infty \cdot A} \quad with \quad q_\infty = \frac{\rho}{2} U^2 \quad and \quad A = chord \cdot span \tag{6.1}$$

- applies a low pass Bessel filter smoothing,
- calculates the damping values for harmonic motion types and
- does some statistical evaluations, when more than one period/event has been measured.

The effort of a full error propagation analysis is not spent here, since the software is under permanent development.

Note: With only F_y and M_z available, the balance was mounted with a clockwise 90° turn around the x-axis. Measured were thus the negative normal force (y-axis pointing down now) and the negative pitching moment (z-axis, now pointing to port). The processing of the second program was altered to cope with this change. Whilst no translation into the aerodynamic coordinate system is possible without a measurement of F_x, the output is reduced to F_N (positive when pointing upward) and M_{pitch} (positive when increasing α) and both their coefficients.

Force Separation

As an example to the force separation prescribed in chapter 2.2, figures 10 and 11 show the normal force and pitching moment before and after the separation with the help of the inertial moment dummy for the *ARinf* model in case I (already filtered). It can be seen that the acceleration peaks at the beginning and end of the motion are effectively eliminated from the remaining aerodynamic force and moment. Still it can bee seen that e.g. in figure 10 at the beginning and in the end of the perching stroke and of the backstroke small local peaks at the acceleration peak positions remain in the resulting aerodynamic force. These small peaks could be interpreted as unphysical remains pointing out some insufficiency of the force separation method. It is also possible that the small peaks come from the hardware issues discussed in chapter 4.1. The occurrence of multi peaks that appear only towards the end of the perching stroke is further discussed in chapter 6.3.

Filtering

The *MGCplus* hardware in charge of amplifying and digitizing the balance and drive data will always carry out a filtering. Since the filtering level shall be decided upon later and carried out by the processing software, the low pass filter frequency in the *MGCplus* was set to the highest possible value of 200Hz in order not to loose any details in the signals. When in the following it is spoken of *unfiltered* values, then the *MGCplus* hardware filtering is not taken into account. The chosen filter frequency is discussed in chapter 6.3

6.3 Results

Plot Generation

The perching motion begins and ends with almost constant angles of attack. For the most precision and for technical reasons, it was found useful to set the trigger point of the force measurements inside the area of “constant” motion in the second half of P (backward move). Once set, the trigger point was kept through the whole force measurement campaign. During data evaluation it was found to be $\bar{\alpha}_{trigger} = 26.34875°$. Therefore the raw data starts at $t_{(\bar{\alpha}_{trigger})} = 0$ but not at t_0.

For a better comparability of the four motion cases, all measured data is plotted over the normalized time axis *t/P* and all plots start at t_0 or *t/P*=0 respectively. To manipulate the time axes in that way, it is necessary to determine the characteristics listed in table 4 from the averaged measurements first. The deviations of the periods and their ratios from the theoretical values of table 2 indicate the measurement accuracy combined with the motion accuracy, which is further discussed in chapter 8. The new time axes are then simply calculated by

$$\left(t/P\right)_{case} = \left(\frac{\overline{t_{raw}} - \overline{t_0}}{\overline{P}}\right)_{case} . \tag{6.2}$$

The mean tag refers to averaging over the 50 single measurement events of each case as well as to averaging over the cases and models where useful. The time can also be expressed in chords being passed with the wind tunnel velocity. The convective time $t_{conv.}$ is then the time for passing one chord. Since the actual wind tunnel velocity is influenced by the blocking of the swivelling model, the time axis translation into chords is carried out via the factor between the ideal period and the ideal convective time.

case	$\overline{\alpha_{(trigger)}}$	$\overline{t_{(\bar{\alpha})}}$	$\overline{t_0}$	$\overline{P}$	$\overline{P_{case}} / \overline{P_I}$	$P / t_{conv.}$
	[°]	[s]	[s]	[s]		[chords]
I	26.34875	0.970908255	0.497803359	1.900094335	1	104.7197551
II	26.34875	1.963567100	1.017356719	3.856045850	2.0294	209.4395102
III	26.34875	2.382837585	1.240859538	4.682347900	2.4643	104.7197551
IV	26.34875	0.970908255	0.497803359	1.900094335	1	209.4395102

Table 4: Time axis transformation values

Vibrations

The figures 12 an 13 hold the averaged unfiltered and filtered measurements of the normal force coefficient and the pitching moment coefficient for each single motion and model. The unfiltered measurements show several superimposed vibrations around the frequencies

- 28.2Hz,
- 35.7Hz,
- 43.5Hz and
- 50.0Hz,

for which the reasons were mentioned in chapter 4.1. The vibrations are much stronger during the motion sections, which points to their mechanical origin. This is also indicated by the fact that higher k values lead to stronger vibrations. To eliminate these frequencies from the data, a low pass filter frequency of 25Hz was chosen. The multiple peak in normal force and pitching moment sometimes visible in the first motion branch (0°→45°) is so far expected to be of physical nature and not one undetected vibration or motion issue. The second motion branch (45°→0°) is not discussed as this investigation is on the perching motion as defined above. However, the backward motion results are also included, since they may be of interest. It is also noticed, that the measurements of the *ARinf* model show a higher vibration level, which may be related to the higher mass. In the motionless sections at the beginning and end of each period the difference from zero of both force and moment coefficients and their variation amongst all measurements is a combined result of the motion precision (see chapter 8) and the accuracy of the prescribed balance measurement methology.

Common Characteristics

The filtered measurements share the following common characteristics:

- Together with the motion start, both the normal force and the pitching moment increase almost linearly with α. (This increase is steeper than the decrease on the backward motion)
- c_N and $c_{M,pitch}$ at almost the same time for each case reach a relative maximum, that is in any tested case higher than the quasi steady state values before the backward motion. This first peak must be directly related to some flow event e.g. a shedding of a vortex.
- The first maximum takes place long before the perching motion is decelerated.
- The first maximum is either followed or not by one or more local maxima at about the same level,
- before a slow decrease to the quasi steady values takes place.

The figures 14 and 15 show the filtered measurements for variations of Reynolds number and constant values of k. Figure 16 is suitable to compare the measurements with variation of k but fixed Reynolds number. The slopes of the *AR2* model are in blue whilst those of the *ARinf* model are red colours.

Influence of the Reynolds Number

Both slopes of c_N and $c_{M,pitch}$ show no clearly identifiable relations between Reynolds number and slope characteristics. For pure variation in Re, the slopes have almost identical

- slope increases,
- peak values, numbers and positions,
- decay durations and
- quasi steady values.

There is a tendency visible, that higher Reynolds numbers result in slightly higher values of the coefficient values (for $\alpha>0$ of course). The normal force slopes of the *ARinf* model in figure 14 are an exception to that tendency. In this case, the values are so close that the exception can be ignored considering the accuracy mentioned above.

Influence of the Reduced Frequency

A strong influence of k can be seen for increasing k values in a

- later (time and alpha) position of the first maximum together with a
- higher peak value and
- a longer lasting decay

of both c_N and $c_{M,pitch}$ slopes.
A possible explanation is a higher and faster energy transfer to an edge vortex, which delays its shedding.

At the same time it is seen that k has

- no influence on the steepness of the normal force slope,

- whilst for the pitching moment slope an increase of k has a small adverse effect on the steepness.

Also,

- k has no influence on quasi steady values, as expected.

Influence of the Wingtip Flow

The comparison of the measurement values of both models may not be mistaken for the comparison of two finite aspect ratios. The *ARinf* model was designed to have the wingtips located in the boundary layers of the sidewalls, which is expected to substantially prevent the formation of wing tip vortices. Therefore the *ARinf* model may work as a wing with infinite aspect ratio, which means it represents the theoretical limit to or prevention of aspect ratio effects. It is obvious that some sort of flow still bypasses the tip edges through the remaining gap of 4mm, as the pressure difference for high angles of attack is large, especially for the high Reynolds Number cases.
The suppression of wing tip vortices clearly causes in both c_N and $c_{M,pitch}$ slopes

- steeper increases,
- earlier events of the first maximum (with a first peak value either lower or about the same level as of the *AR2* model),
- the appearance of multiple peaks (debateable!, see below.) and
- higher quasi steady values.

Multiple Peaks

The origin of multiple peaks towards the end of the perching stroke can be speculated about: The force measurements alone cannot prove nor deny that the multiple peaks remaining after the chosen low pass filtering and force separation method are caused by aerodynamic events. Their lack of appearance in the measurements of the AR2 model could be taken as indication of some mechanical event taking place with some lower frequency (due to the higher mass) then the ones identified. The unfiltered plots show that the vibration level is high only during the motion stages, but there such low frequencies couldn't be detected. It is also possible that the low frequency of the multiple peaks is a beat frequency with no

physical background that is generated during the force separation in the case that the two signals to be subtracted have some time phase error (see chapter 8). On the other hand, it is just as conceivable, that the multiple peaks are related to one or more aerodynamic events, like e.g. the formation, combination or shedding of a leading and a trailing edge vortex or a stall with some small time in between. The suppression of the wing tip vortex formation with the ARinf model could have caused or strengthened such events. The following examination of the flow field with PIV was carried out to get deeper insight into that issue.

7 PIV Measurements

7.1 Selection of Time Stages

After looking over the force measurements, it was decided to have a close investigation of motion case I carried out with the *ARinf* model, to gain insight of the force development by recording the corresponding 2D flow fields on several characteristic time stages. The time stages are listed in table 5 and shown in figure 17. Points ① and ⑦ represent the quasi steady stages. Point ② is seated at ½ of the first maximum force whilst point ③ is chosen at the first maximum, which happens to take place when half of the pitch stroke was executed for this case. Point ④ is placed at the backstroke of the force and point ⑤ on the second maximum. Point ⑥ represents the middle of the force decay after the full stroke was executed.

time stage	note	relative span wise laser plane position	trigger time related to half pitch stroke	trigger time related to half wait stage before motion ($t_0=0$)	α (Eq 3.2)
			[s]	[s]	[°]
①	quasi steady start at α=0°	1/3	-0.300	0.173	0.0
②	half of maximum force	1/3	-0.060	0.413	11.1
③	1st rel. max force and half pitch stroke	1/3 and 2/3	0.000	0.473	22.5
④	1st rel. min force	1/3	0.040	0.513	30.1
⑤	2nd rel. max force	1/3	0.085	0.558	38.6
⑥	force and vibrations decay	1/3	0.340	0.813	45.0
⑦	quasi steady end at α=45°	1/3 and 2/3	0.740	1.213	45.0

Table 5: Measurement points of motion case I for PIV

7.2 Measurement Setup

Figure 18 shows the measurement setup for 2D PIV in vertical slices across the wingspan. It was favourable to shoot the pictures through the right wall of the test section (from starboard) and to have the laser plane enter the test section from underneath. Therefore the motion was carried out upside down with alpha going from 0° to -45°. The measurement plane was illuminated by a pair of *nanoPIV* lasers from *Litron Lasers Ltd.*. The lasers are of Nd:YAG type and emit 4ns long pulses of 1064.5nm wavelength. A *pco.4000* camera of *PCO AG* with a resolution of 4008x2672 pixel and 14bit greyscale was used together with a *Carl ZEISS AG MAKRO-Planar T*2/50mmZF* lens to record the double images. Camera and lasers were mounted on the same mechanical support, so that for all pictures taken at one span position the same viewpoint and scale was kept. All time stages were measured at 1/3 span and two reference measurements were taken also at 2/3 span for checking on 3D effects. The optical resolution for the 1/3 span plane was 0.0617mm/pixel. The switch of the PIV setup from the 1/3 span to the 2/3 span position caused a slight change in resolution and viewpoint. At 2/3 span, the resolution was 0.0631mm/pixel. For each measurement point a number of 700 double pictures were taken to account for the high unsteadiness of the flow field and to assure reliable statistical data of the turbulent properties. The trigger setup for recording the mentioned time stages consisted of a light barrier and a *Model DG 535* time delay device from *Stanford Research Systems Inc.*. The trigger signal was fed into a recording system of *LaVision GmbH* with a *V9.0 triggerPTU* programmable timing unit, that controls the lasers and camera. A time of $\Delta t_{pulse} = 70\mu s$ between the two laser pulses was found to be the best

trade-off for measuring velocities inside and outside the separated areas. Longer times would theoretically have lead to a higher accuracy inside via larger particle translations but in praxis only lead to too much loss of particles due to out of plane motion.

Trigger Accuracy

The trigger light barrier was placed at the middle of the motion path of the second drive (thus also at the middle of the motion). The position was fine tuned by measuring the durations of the two half motions, one above and one below the light barrier until a difference of only 0.5×10^{-4}s was left. Then the difference between the pictures taken for the two motion directions could be averaged to $\Delta\alpha = 2x0.75°$, which - with the maximum motion velocity of $\dot{\alpha}$=190.23°/s - indicates a dead time for the trigger system of $\Delta t_{dead} = 0.004s$. This dead time was used to correct the trigger points of all recorded time stages.

Plot Generation

The plots of the PIV planes were made with inverted x- and y-axes to have the common viewpoint from port and positive alpha indicating up. This processing does not affect the sign of the rotational values like e.g. vorticity etc.. With the mentioned back and forth translation during rotational motions, the x-position of the rotational centre, the 1/4 chord point, is not constant during the different time stages. Table 6 holds the surface coordinates of the ¼-chord point on the suction side taken from the PIV calibration pictures. These coordinates together with the ideal angle of attack (from Eq. 3.2) were used to position a drawing of the airfoil into the 2D-plots. The change in the y-position of the rotational centre is caused by two aspects:
a) the positioning of the optical axis below the wing (above in the plots) to assure a free view up to the surface and
b) small geometric errors in the CAD representation of the motion simulation in the very beginning of the motion programming process (which is identified as a subject of future improvements).

time stage	relative span wise laser plane position	x-position on the suction surface	y-position on the suction surface	optical resolution	α (Eq 3.2)
		[mm]	[mm]	[mm/pixel]	[°]
①	1/3	0	0	0.0617	0.0
②	1/3	10.92	4.63	0.0617	11.1
③	1/3	10.49	5.12	0.0617	22.5
④	1/3	2.28	4.50	0.0617	30.1
⑤	1/3	-15.11	4.01	0.0617	38.6
⑥	1/3	-37.75	0.68	0.0617	45.0
⑦	1/3	-37.75	0.68	0.0617	45.0
③	2/3	10.11	4.05	0.0631	22.5
⑦	2/3	-38.50	-0.38	0.0631	45.0

Table 6: Surface coordinates of the rotational centre (1/4 chord point)

7.3 Processing and Quality

The double pictures were processed with *DaVis 7.2.2.393* version of *LaVision GmbH*. The processing consists of the following steps:

1. Masking out the laser surface line, shadowed areas and those areas, where the picture quality didn't allow for a reasonable velocity determination.
2. Subtraction of the average local brightness to eliminate reflections from the fuselage etc..
3. Vector determination was carried out with the offered second order multi-grid and multi-pass correlation algorithm. The final interrogation window size of 32x32 pixel and 50% overlap lead together with the scale factor to a local vector resolution of 0.987mm.
4. Post processing the found vector fields by replacing those vectors that misfit certain confidence aspects (a difference of more than 600% from their neighbour's RMS values) and finally a 3x3 smoothing of the vector field.
5. Performing a statistical analysis of the post processed vector fields that delivers average velocities, standard deviations, 2D strains and turbulent energy.

For further details of the processing software, the manual and prescriptions available on the internet site of *LaVision GmbH* is referenced (www.lavision.com). All pictures taken as well as the single vector fields and the processing parameters are stored on the data medium attached to this report so that a later processing of different kind can be carried out.

The accuracy of such a complex measurement process carried out with 3rd party software can hardly be evaluated in the classical analytic error propagation manner. In addition to the accuracy statements of *LaVision GmbH*, in this report the 2D distribution of peak ratio values (first to second peak for each interrogation window) determined during step 3 is considered to be an adequate measure to rate the local quality of the PIV. Figure 19 shows these value distributions for all time stages. It can be seen that in general the process quality decreases towards the lower plot border (upper border of the raw data) below the model (pressure side). One of the lasers was only capable of emitting about 30% of its specified intensity, so the setup was optimized for illumination of the suction side. It is also visible by the peak ratio values, that the quality inside the separation (especially at its border, where shear is intense) and in the wake region is lower than outside. The latter two are an inevitable characteristic of disturbed and turbulent areas caused by out of plane motions of the particles.

7.4 Results

The figures 20 to 28 hold the average velocity fields and in smaller sizes and resolution a single velocity fields of four recorded events (100, 200, 300 and 400 out of 700) to demonstrate the variation of the flow field.
The figures 29 to 37 show the RMS values of the velocity and the Reynolds stress distribution $u'v'/U_\infty^2$ as an extract of the statistically derived data. Further data is stored in the *DaVis* solutions on the external storage device (in *LaVision's* proprietary *.im7* file format).

Stage 1 at 1/3 Span

Stage ① is the quasi steady state at $\alpha = 0°$. The average velocity field looks as one would expect: The flow is in general parallel, very smooth around the wing and has a flat wake

area. In that area, the single event figures show that the Karman vortex street is captured by the PIV.

As in stage ① the flow has to be symmetric to the chord, one can judge in accordance to the peak ratio conclusions also from the single event recordings, the RMS values and the Reynolds stress u´v´ distribution that the process quality on the lower side of the picture area is decreasing towards the picture bottom. This is to be kept in mind when looking at the following stages.

Stage 2 at 1/3 Span

At stage ②, which takes place at about 1/4 of the perch stroke, already more than 50% of the maximum normal force were measured. The streamlines are considerably bent near the leading edge but no separation takes place and no vortex appears neither in the averaged nor in the single event recordings. The Karman vortex street is still persistent in the single event recordings.

Low process quality on the lower side upstream and in the lower right edge of the plot is evident again in the RMS values and Reynolds stress components.

Stage 3 at 1/3 Span

Stage ③ marks the point of maximum normal force and pitching moment recorded. The average flow field shows a large, closed, homogenous separation filled with a single vortex . Its centre is located over 1/2 chord at 1/4 chord distance to the surface. The RMS values in the vortex are high, especially near the centre and in the shear area along the separation streamline. Strong negative values of u´v´ are found in most the vortex area whilst positive values cover large parts of the wing surface. A strong velocity surplus is found above the first half of the separation. The single event recordings show strong deviations from the average flow field like a frayed out border of the in average clearly defined separation area and many small, weak vortices inside the separation.

Stage 4 at 1/3 Span

At stage ④ the first relative minimum in normal force and pitching moment was recorded. The average velocity field here has changed dramatically from stage ③: Three vortices are now consistent in the average field. The strongest of them is the trailing edge vortex (thus turning positively) seated very near the surface. It is feed by high surplus velocities in the trailing edge flow coming from the lower wing side, which are characterized by large u´v´ values. The other two vortices are turning negatively and produce negative u´v´. One is the leading edge vortex, which happens to be seated around the 1/4 chord point in a distance of 1/4 chord to the surface. It is driven by the flow around the leading edge. The third is seated above 2/3 chord and has a surface distance of 1/2 chord. This one is feed from the trailing edge vortex from the right side and from the shear layer above. The system draws material from the wake region inside in between the central vortex and the tailing edge vortex. The single event recordings show a much more shredded separation field. However, the trailing edge vortex can always be identified.

With the velocity field topology of stages ③ and ⑤ (see below) looking similar and the one of stage ④ differing drastically from those two, it could be deduced that this topology difference

is the reason behind the local minimum of the pitching moment, as the local peaks of the pitching moment were in good sync with the PIV time stages ③ to ⑤. Unfortunately, a positive turning trailing edge vortex, which is the unique/outstanding flow feature of stage ④, puts – in the opinion of the author - force on the surface with the lever of about 3/4 chord, which should increase the pitching moment but not cause a local minimum. Thus, a large, single vortex like in stages ③ to ⑤ has to be more effective on that task than the trailing edge vortex in stage ④, which may be adverse to the strength of the leading edge vortex, so that in sum (leading edge vortex pulls, trailing edge vortex pushes around 1/4 chord reference point) a lower pitching moment is created.

Stage 5 at 1/3 Span

Stage ⑤ was placed to the second relative maximum of the normal force and the pitching moment were recorded. As figure 17 shows, these two maxima are not in sync. Actually stage ⑤ is right on line with the second maximum of the moment but too late for the second force maximum – actually it is placed nearer to the second relative force minimum.
The average velocity field is dominated by a very large (full chord long and maximal 2/3 chords high) but still closed separation consisting of a strong (fast) single vortex. The centre is located above 2/3 chord at a surface distance of 1/2 chord. The vortex area is dominated by negative u´v´ values except in the vicinity of the leading edge. The single event recordings again do not show such a homogenous inner of the separation but the large vortex is always identifiable with its centre near the average position.

The large single vortex flow analogue to stage ③ puts constant force on the surface near the trailing edge whilst it generates a pull near the leading edge. This is a coherent explanation for the local maxima in pitching moment at both stages ③, and ⑤.

Stages 6 and 7 at 1/3 Span

Stage ⑥ was placed in the force and moment decay with values still a bit higher than stage ⑦, which marks the quasi steady state of maximum attack angle. In fact both velocity fields (also both average and single event measurements) look very similar and share the following characteristics: The average field shows a large separation, which reaches past the recorded area may be closed or not. The streamlines are bent negatively so that a possible vortex centre could be seated shortly outside the visible area, far (>1 chord length) from the surface. Positive u´v´ is found near the leading edge quickly followed by a large strong negative u´v´ values along the shear area. Stage ⑦ differs from stage ⑥ in that is shows a negative u´v´ value area after the trailing edge at the lower right edge of the recorded picture, where in stage ⑥ an area of strong positive Reynolds stresses can be found . This however is the same area, which was identified to deliver false values, so no further notice is spent here.

In sum, the higher force and moment values of stage ⑥ over stage ⑦ do not reflect in the flow topology (and could probably better be identified by an averaged pressure field instead of a velocity field).

3D Effects

Stages ③ and ⑦ were recorded also at 2/3 span to check for 3D effects.

At 2/3 span, stage ③ shows a flow field that differs considerably from the one of 1/3 span: The separated area of the average flow field is smaller. It closes at about 1/2 chord and is only about 1/4 chord tall. It too holds a single negatively spinning vortex. Its centre is located above 1/3 chord at a surface distance of 1/8 chord. High RMS values downstream the closure show that this bubble length fluctuates. The single event recordings show no persistent single vortex centre inside the separation nor a clearly defined closure of the separation. Also, no shedding of vortices can be detected through the 700 single recordings.

The flow field at 2/3 span of stage ⑦ shows in average an almost identical shape of the separated area, whilst the inner topology differs: At 2/3 span the stream lines are not bent around a vertex centre but around a source point that is located inside the recorded area at about 1/4 span above the trailing edge. Although a source point inside a 2D cut plane of a separated area is not unphysical, in this case the RMS values distribution and also the single event measurements (e.g. event number 100) - as mentioned - indicate this to be possibly caused by local poor processing quality, so it is not discussed any further.

In sum, the existence of 3D effects here is proven.

3D effects are commonly known for steady state 2D experiments especially inside closed separations (e.g. owl-eyed back flow centres) and their size and influence appears to be somewhat proportional to the ratio between the chord wise separation extend and the wingspan. So it is not irritating to find them also in this experiment with a relatively low reduced frequency k.

8 Motion Precision

The results of the measurements carried out within this campaign reflect a combination of the accuracy of the measurement instruments and the accuracy of the motion carried out. This chapter will judge upon the motion accuracy of the MAVlab mechanism as if the measurement instruments were without error. This compromise is made with the assumption/knowledge, that the accuracy of the instruments surpasses that of the mechanism. For a better differentiation, the accuracy of the mechanism is called *precision* in the following context.

The motion precision is defined by two aspects: The absolute positioning precision and the repetitive/relative precision between consecutive periods of a motion.
Two kind of measurements were carried out, from which both precision types may be judged upon:

a) The force measurements, for which the drive positions were recorded from the same optical position sensor that is used by the motion controller and

b) the PIV, during which pictures of a millimetre grid mounted on the model were taken for calibration also the time of the perch stroke as well as of the back stroke were measured.

Motion Precision by Force Measurement Instrumentation

From the averaged (over 50 strokes) drive positions during the force measurements, the angle of attack of the specimen is calculated out of the recorded positions using the same part dimensions as the CAD simulation used for the programming procedure. This is done exemplarily for case I, which was also the subject of the later PIV measurement. Since the case was recorded 6 times (two with wind tunnel off, one on, each for model *AR2* and *ARinf*), the 6 slopes in figure 38 deliver a good overview of the absolute positioning precision. A comparison with the programmed slope stemming from equation 3.2, which was the input for the programming process should be included in future versions of the recording/processing software. For judging upon the repetitive precision, statistical analysis too needs to be implemented. Whilst the vibrations in the position signal were already discussed in chapter 4.3, here the global characteristics of the motion are judged by the filtered slopes.

Absolute precision:
It can be seen from the alpha recordings, that all slopes show a too low amplitude with alphas starting at 0.1° and only reaching up to 44.8. This value is 1.5 times higher than the design target of the mechanism, but still only 0.7% below the wanted full stroke and thereby acceptable. Since the amplitudes of the drives were fine tuned prior to the measurements, this systematic error is directly related to small errors in the dimensions of the virtual parts of the simulation and could be eliminated by correction of the simulation.
The positions of the mid stroke points reveal that the period carried out is too long. The average period of all recordings was measured 0.0077s or 0.41% larger than the ideal Period, which is also an acceptable value but has to be (and was) taken into account when defining the trigger points of specific stages.

Repetitive precision:
All six recorded slopes agree very well with each other, as the zoomed plots reveal. During the motionless sections, the difference in amplitude amongst them is within 0.1°, which is 50% smaller than the design target. During the sections of constant speed near the half

stroke points all slopes vary only within a range of 0.07° or 0.0002s (3.5 times lower than the design target).

Motion Precision by PIV Measurement Instrumentation

From the recordings during the force measurements alone, one could judge the motion precision to be very satisfying. The angles taken out of the PIV pictures however revealed a problem in the absolute position precision. For each time stage of table 5, pictures were taken with the fine tuned setup and the angle of attack was measured (the angle of the laser surface line against the water balanced picture frame) via the image processing software *corel DRAW X4*.
The absolute positioning precision was found to have a maximum error of about -1.6°, which is 16 times the design target. An error in space of 1.6° is equivalent to an error in time of 0.0084s on the constant velocity section of case I.
The repetitive precision on the other hand appeared to be very good - that is - better than one could measure with the chosen image processing software setup for a test series over 10 consecutive strokes (see the calibration images on the storage device).
The high precision time measurements carried out with the trigger device of the PIV system then revealed that:

a) The times for the upstroke and down stroke varied each time the mechanism was switched off and recalibrated again, whilst their sum remained quite constant.

b) During continuous motion, a small drift in the two stroke times (again with a constant sum) took place over the total amount of 700 consecutive strokes during one full PIV measurement session.

It was found that irregular sensing by the proximity switches used for position calibration was the reason to effect a): The calibrated starting position of the drives was misaligned to the position of the light barrier of the PIV trigger. The maximum error of 1.6° is thus a combination of an error in absolute position and trigger time and the error in levelling the PIV camera with a water balance against its housing. A more precise replacement of the proximity switches in the future is therefore recommended.

The reasons for the drift in the repetitive precision still needs to be found. As to the author's knowledge, the controller uses the input of absolute position data (after once being calibrated), so that a systematic drift in the motion centre cannot be explained and should be further investigated.

A Figures

Fig. 1: LNB windtunnel

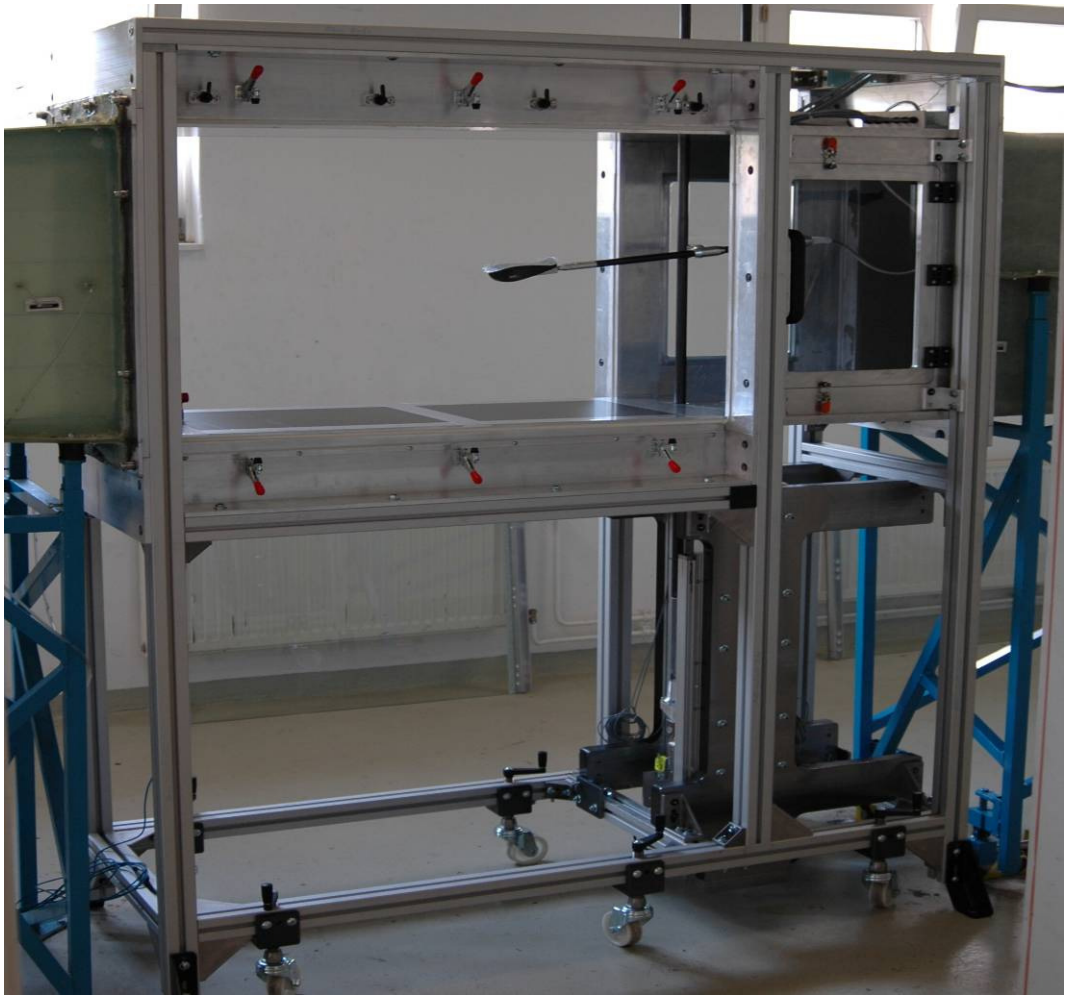

Fig. 2: Dynamic model support

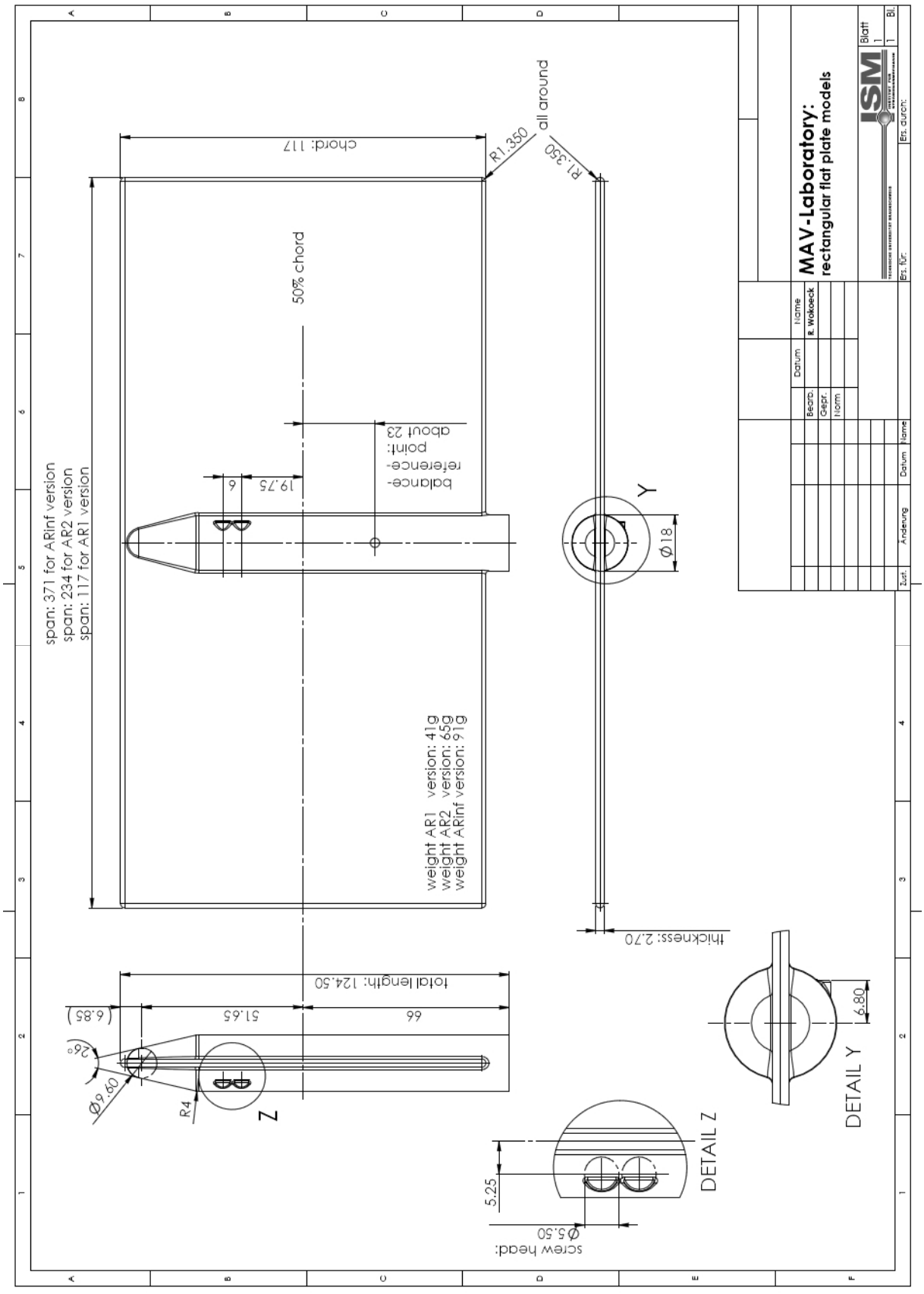
MAV-Laboratory:
rectangular flat plate models
span: 371 for ARInf version
span: 234 for AR2 version
span: 117 for AR1 version
chord: 117
R1.350
all around
50% chord
balance-reference-point: about 23
19.75
6
Y
Ø18
weight AR1 version: 41g
weight AR2 version: 65g
weight ARInf version: 91g
thickness: 2.70
total length: 124.50
(6.85)
51.65
66
26°
Ø9.60
R4
Z
DETAIL Y
6.80
DETAIL Z
5.25
Ø5.50
screw head:

Fig. 3: Models

Fig. 4: Inertial dummies
(left: AR2-version, right: universal/ARinf-version)

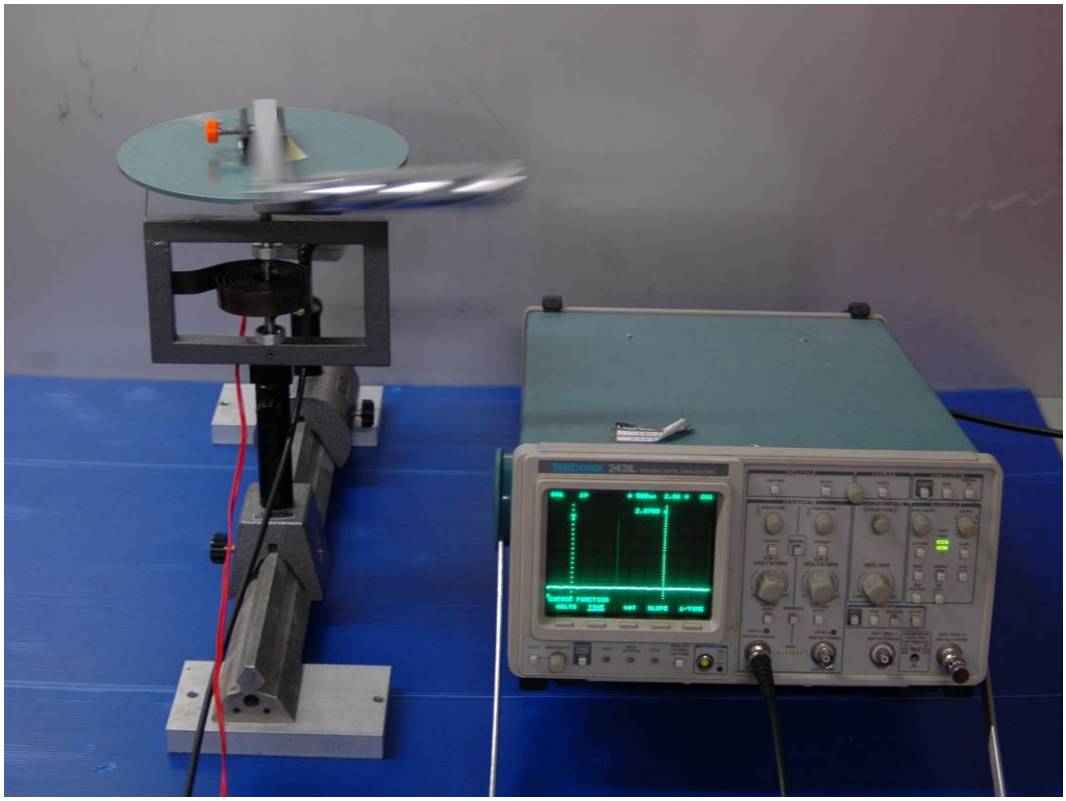

Fig. 5: Inertial momentum test stand

Fig. 6: Reused sting and chopped off head.

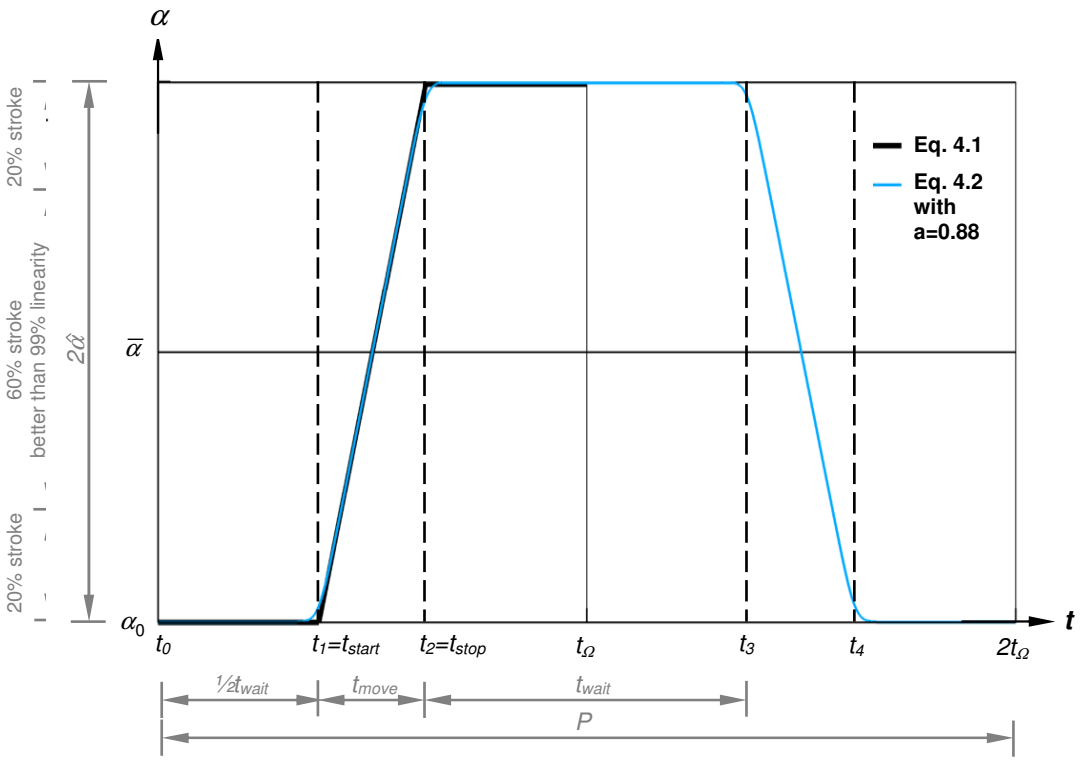

Fig. 7: Perching motion graphs

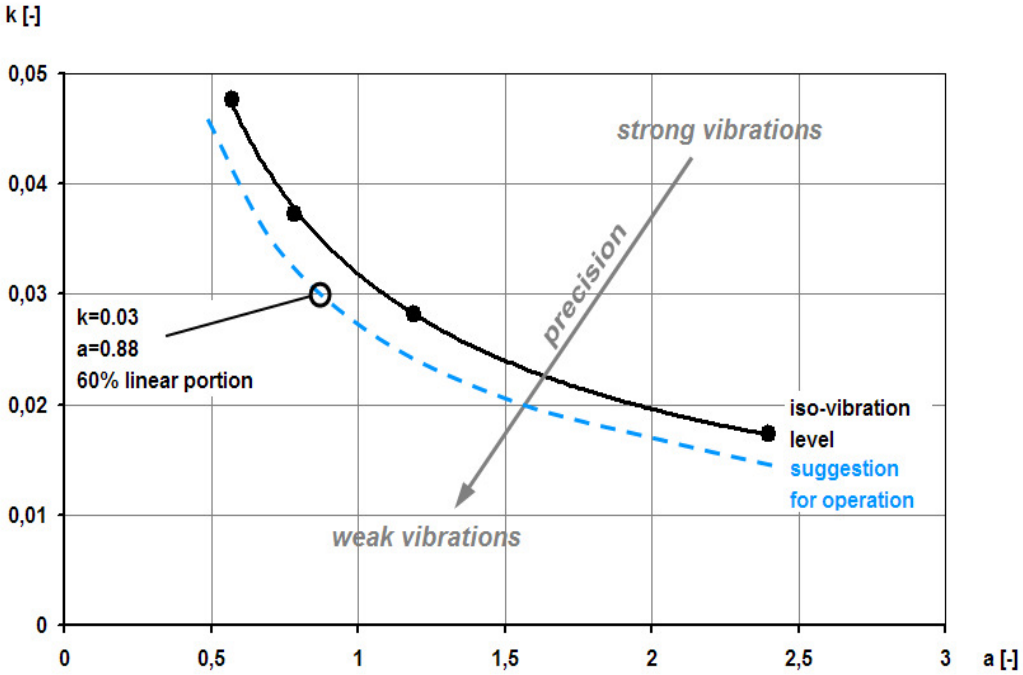

Fig. 8: Operation domain restricted by vibration level

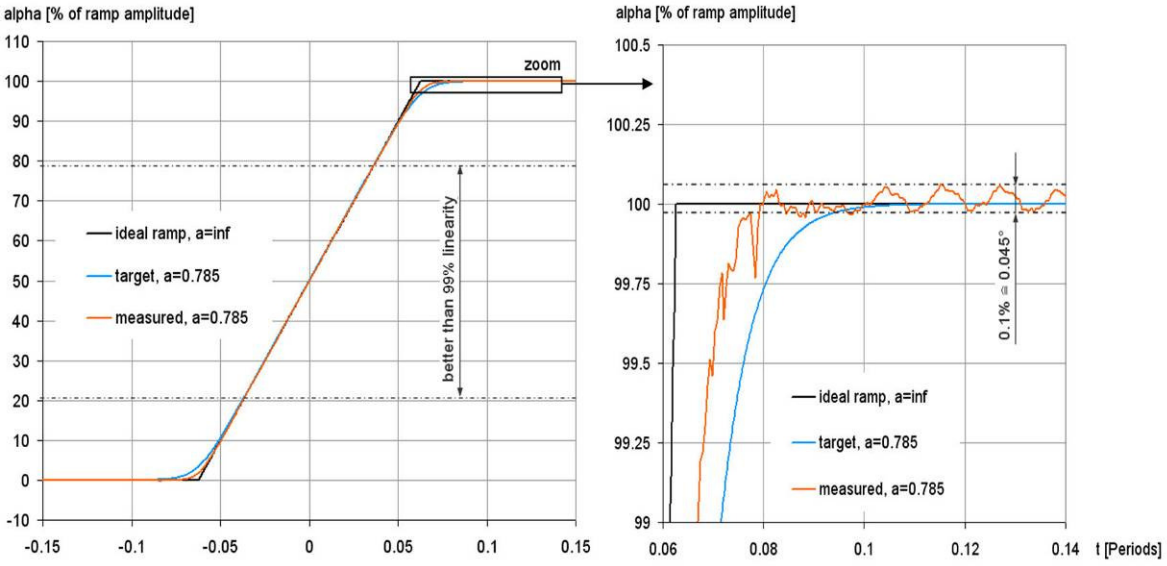

Figure 9: Perching motion accuracy found in prior tests

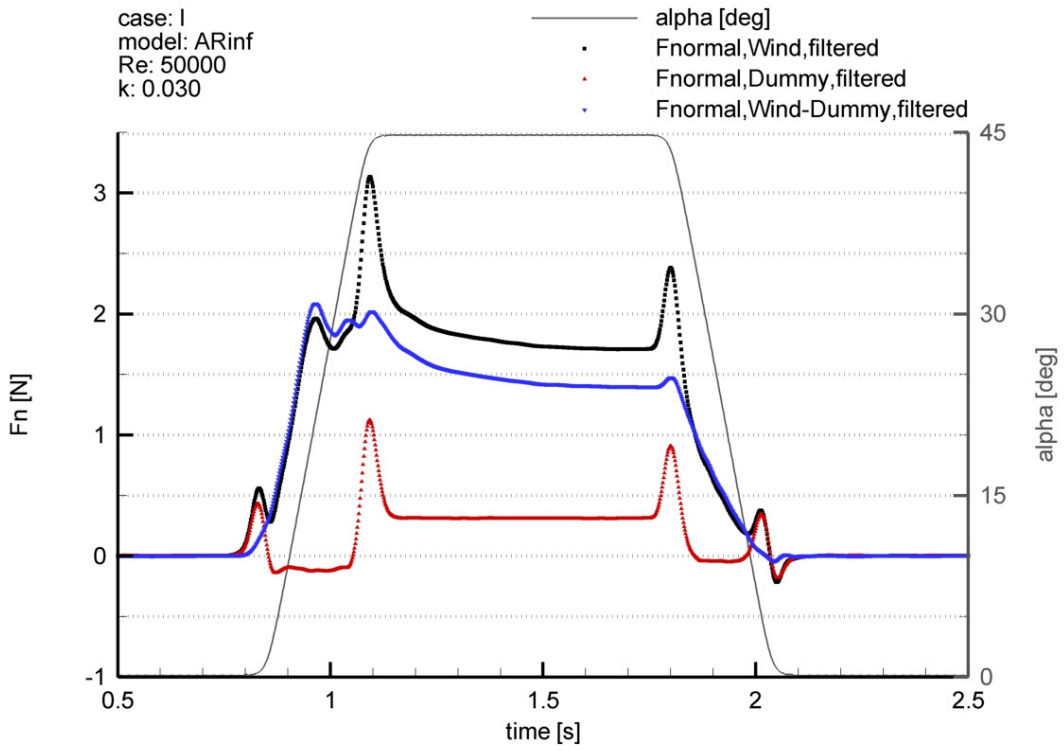

Figure 10: Force separation shown for F_N, case I, *ARinf* model
(Low pass Bessel filter frequency: 25Hz)

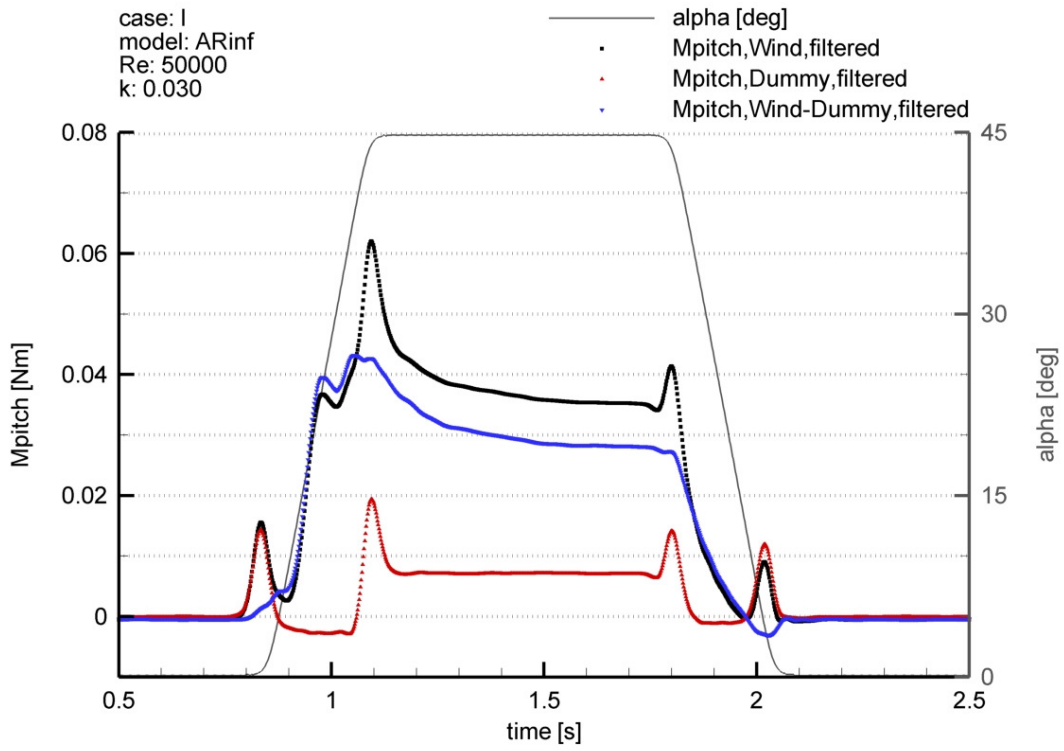

Figure 11: Force separation shown for M_{pitch}, case I, *ARinf* model
(Low pass Bessel filter frequency: 25Hz)

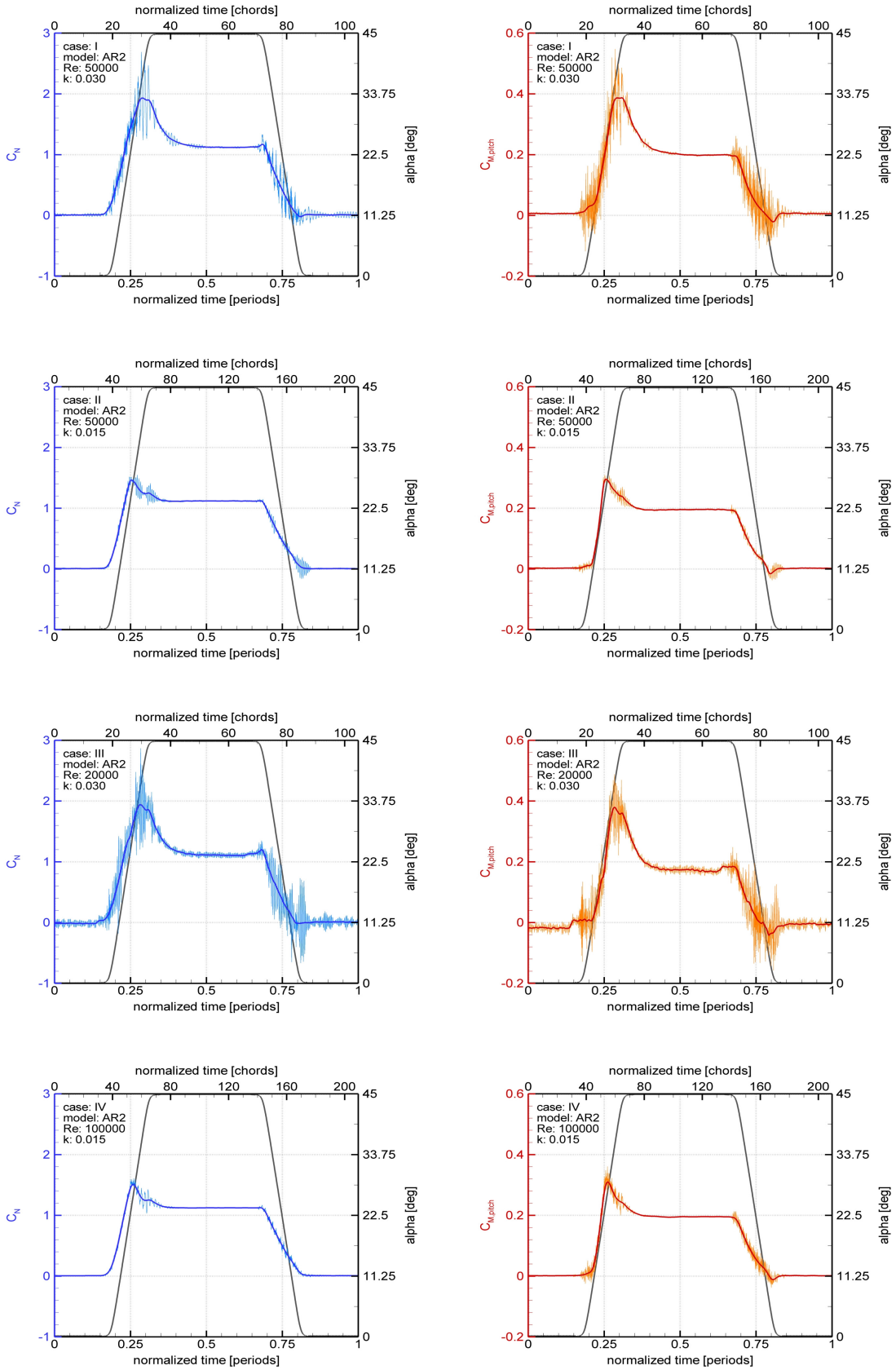

Figure 12: Force and momentum measurements of the *AR2* model.
(Low pass Bessel filter frequencies: 200Hz and 25Hz)

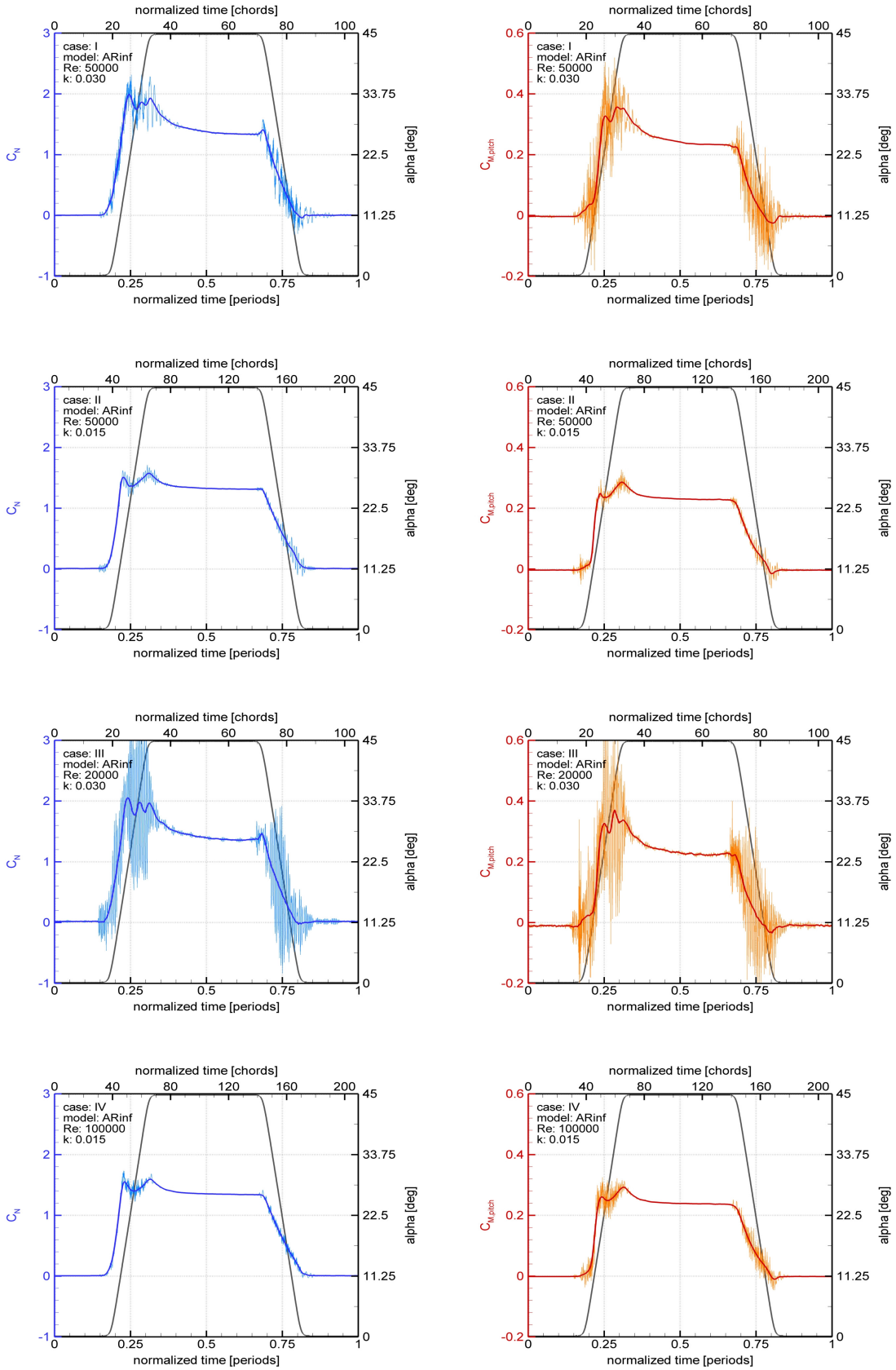

Figure 13: Force and momentum measurements of the *ARinf* model (Low pass Bessel filter frequencies: 200Hz and 25Hz)

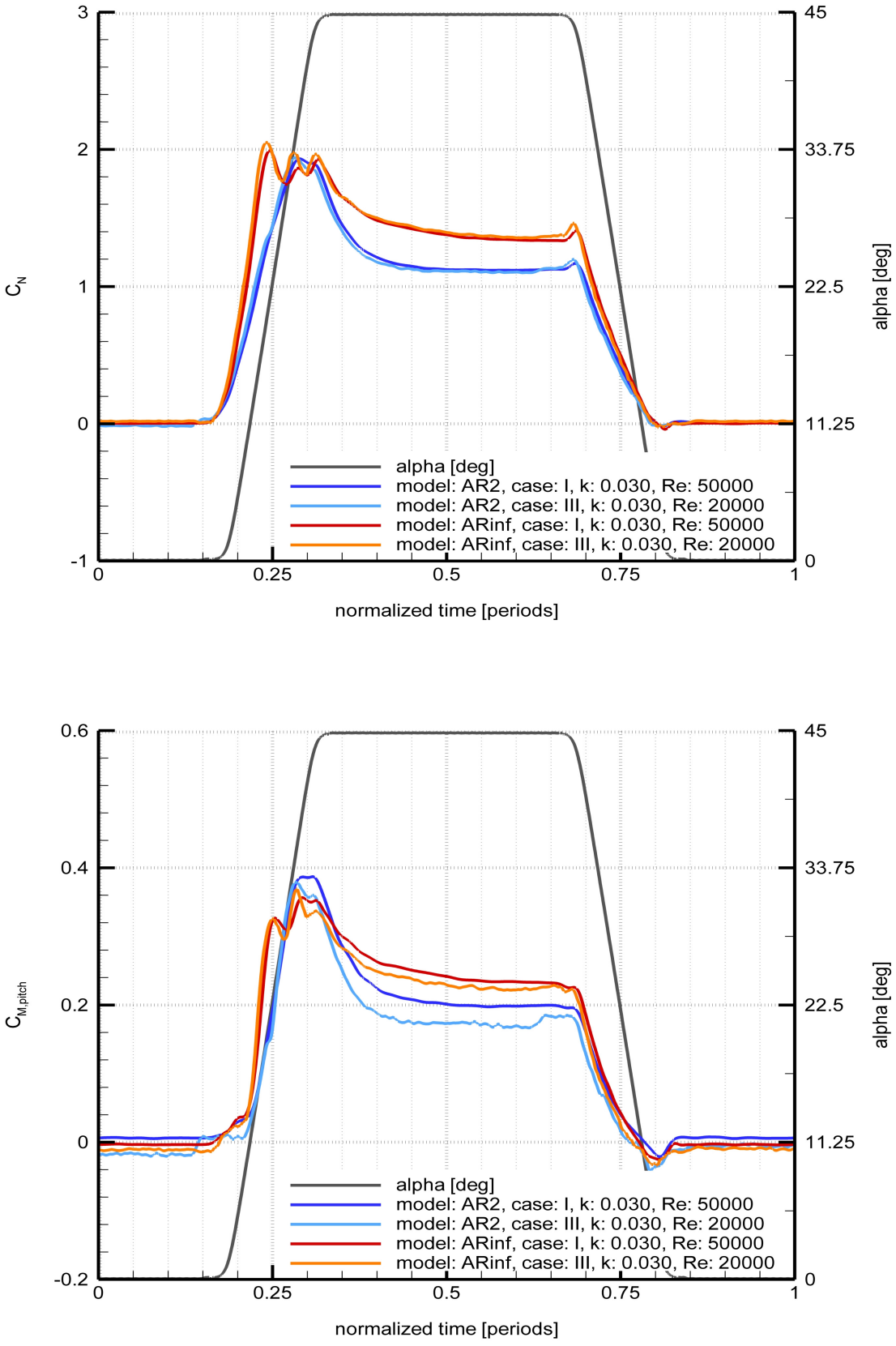

Figure 14: Force and momentum measurements with k=0.030
(Low pass Bessel filter frequency: 25Hz)

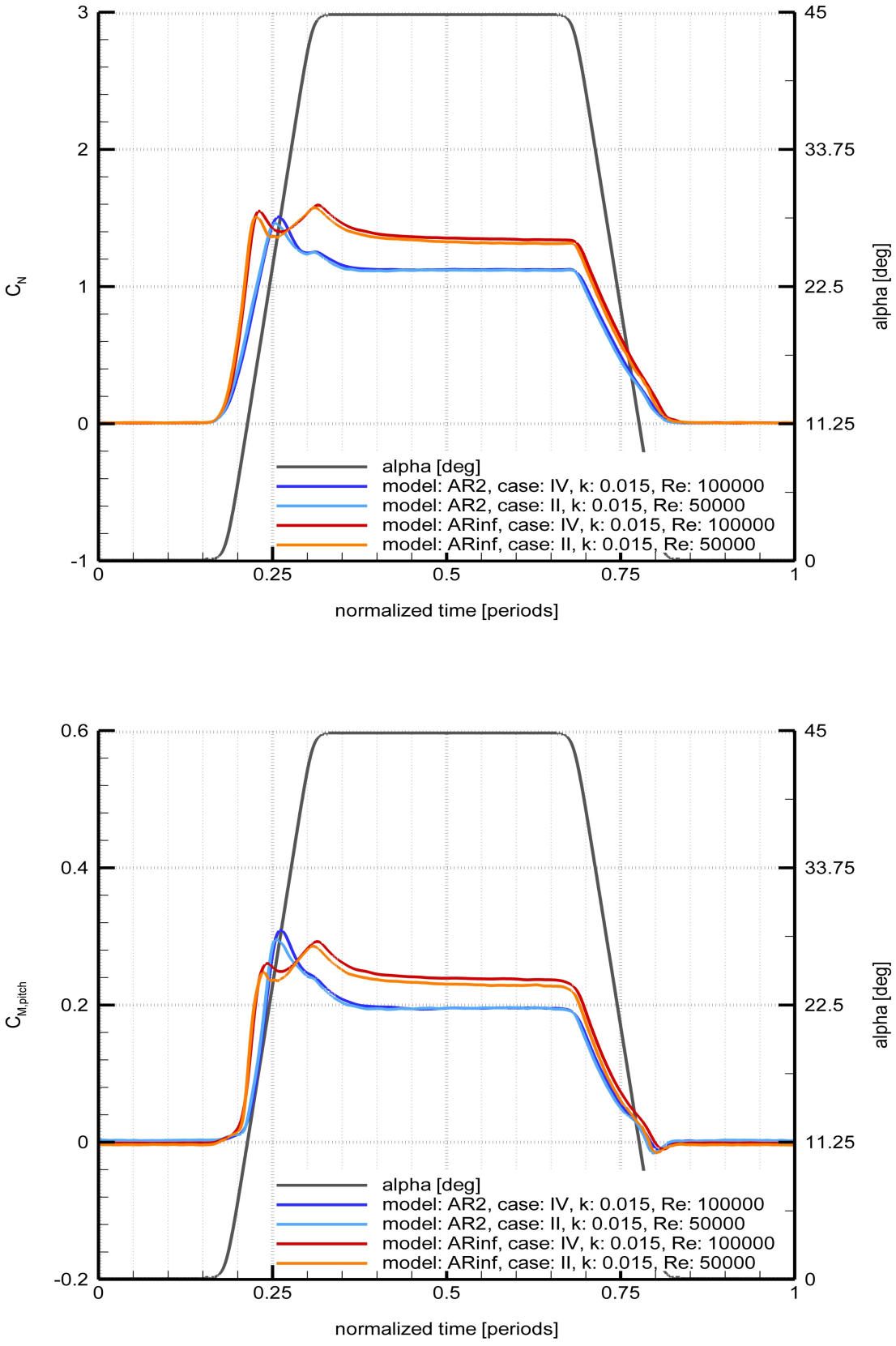

Figure 15: Force and momentum measurements with k=0.015
(Low pass Bessel filter frequency: 25Hz)

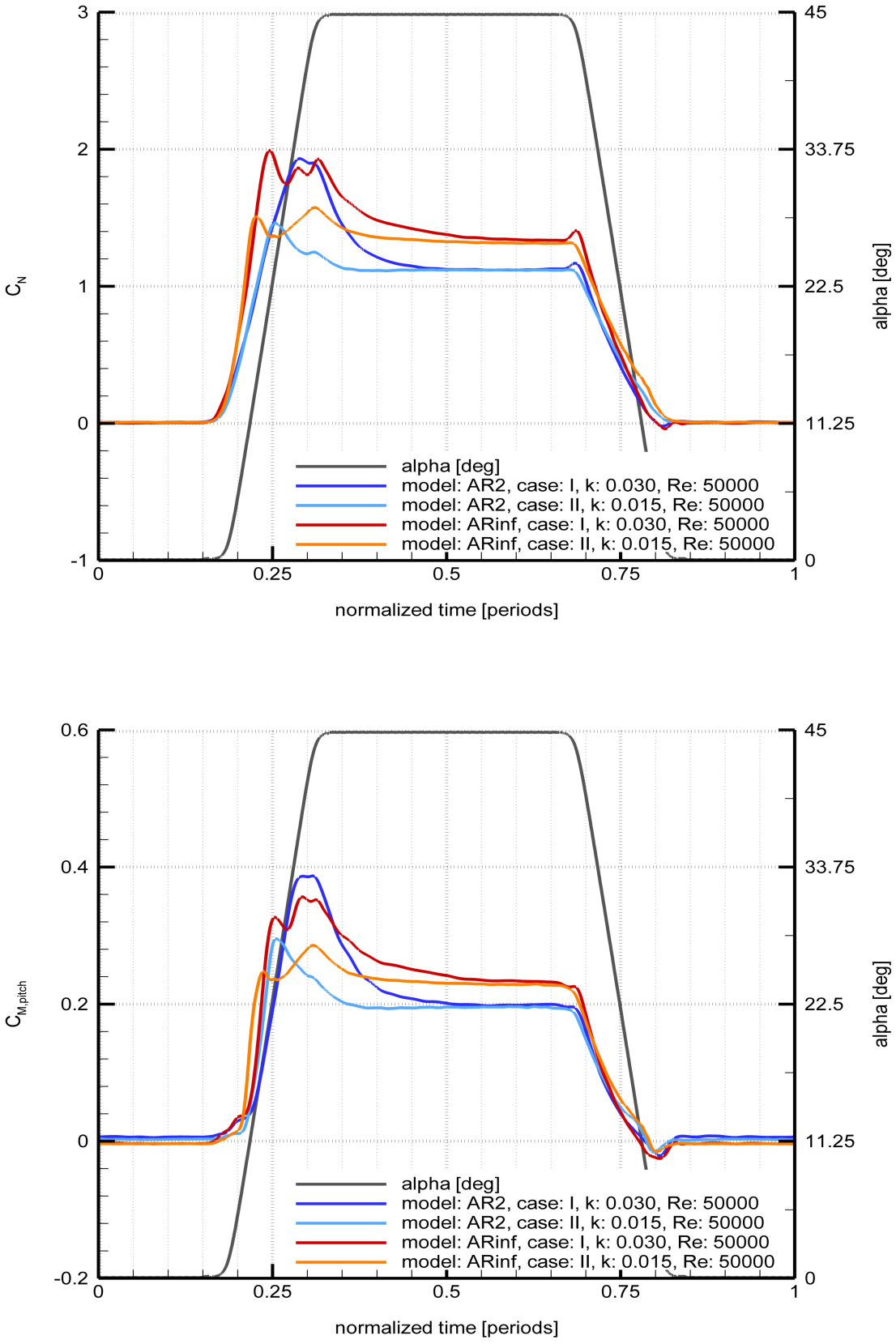

Figure 16: Force and momentum measurements with Re=50000
(Low pass Bessel filter frequency: 25Hz)

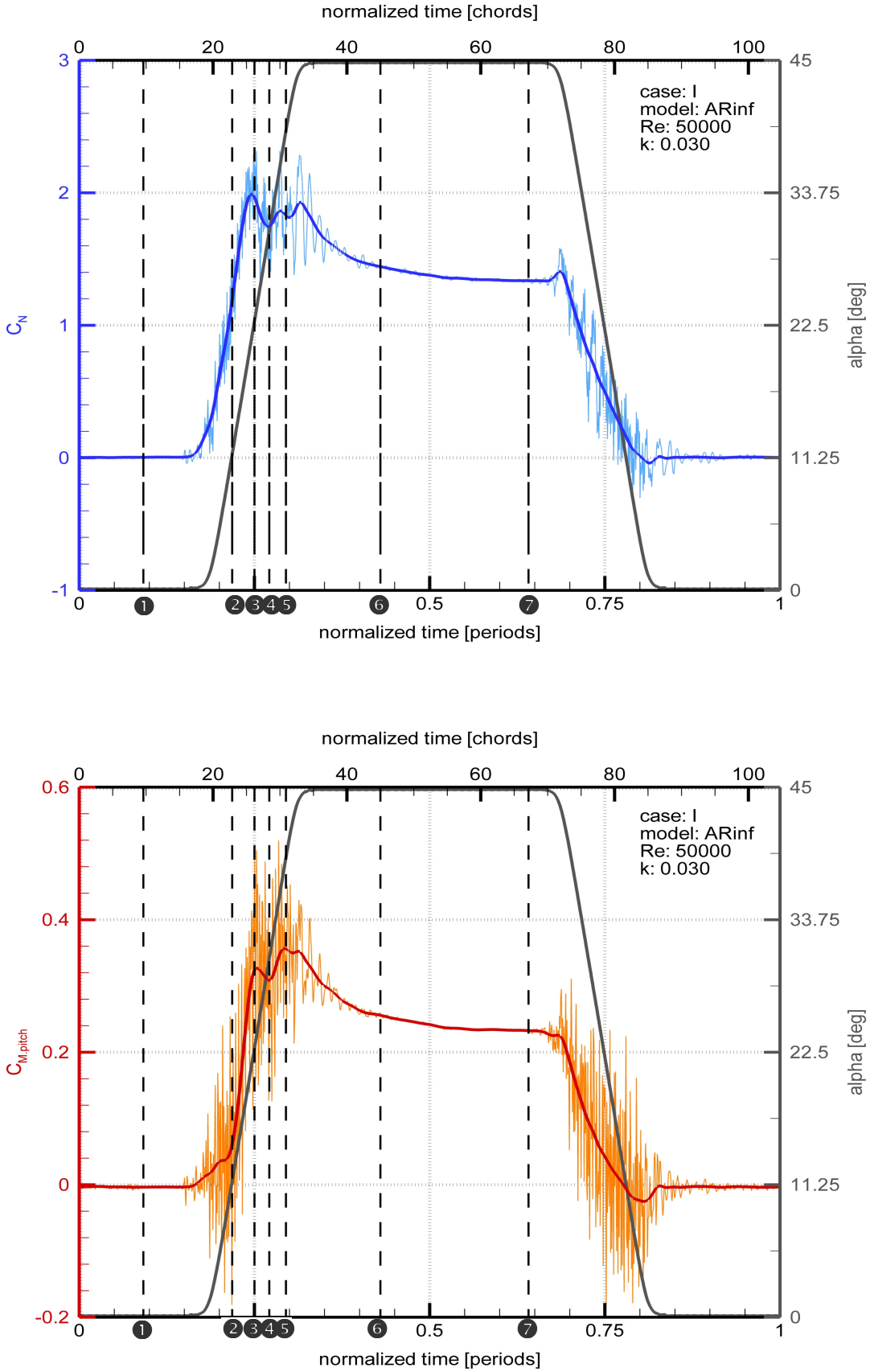

Figure 17: Position of PIV time stages selected from the force and momentum measurements of case I with *ARinf* model
(Low pass Bessel filter frequencies: 200Hz and 25Hz)

Figure 18: PIV setup

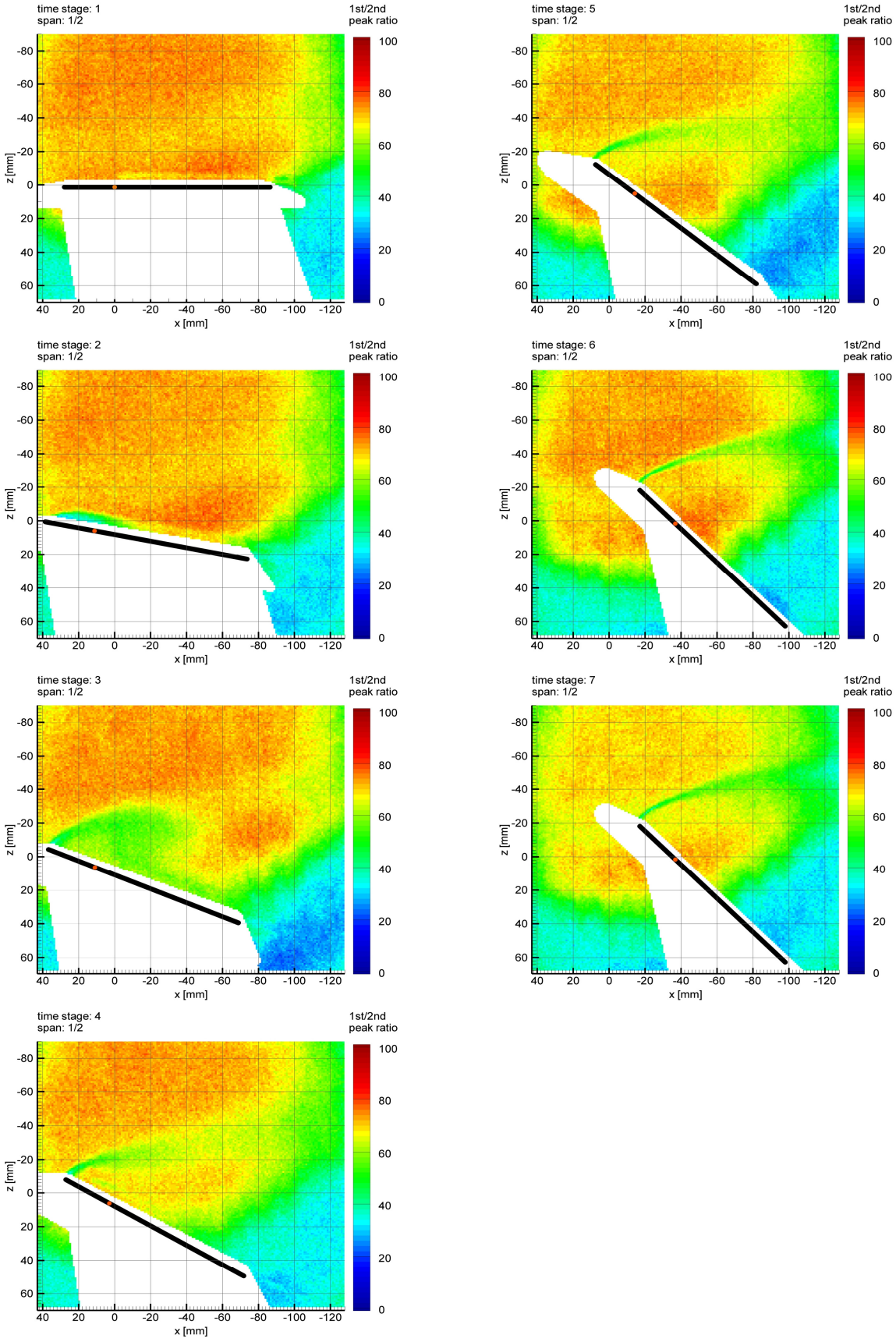

Figure 19: Average 1st to 2nd peak ratio distributions during PIV evaluation

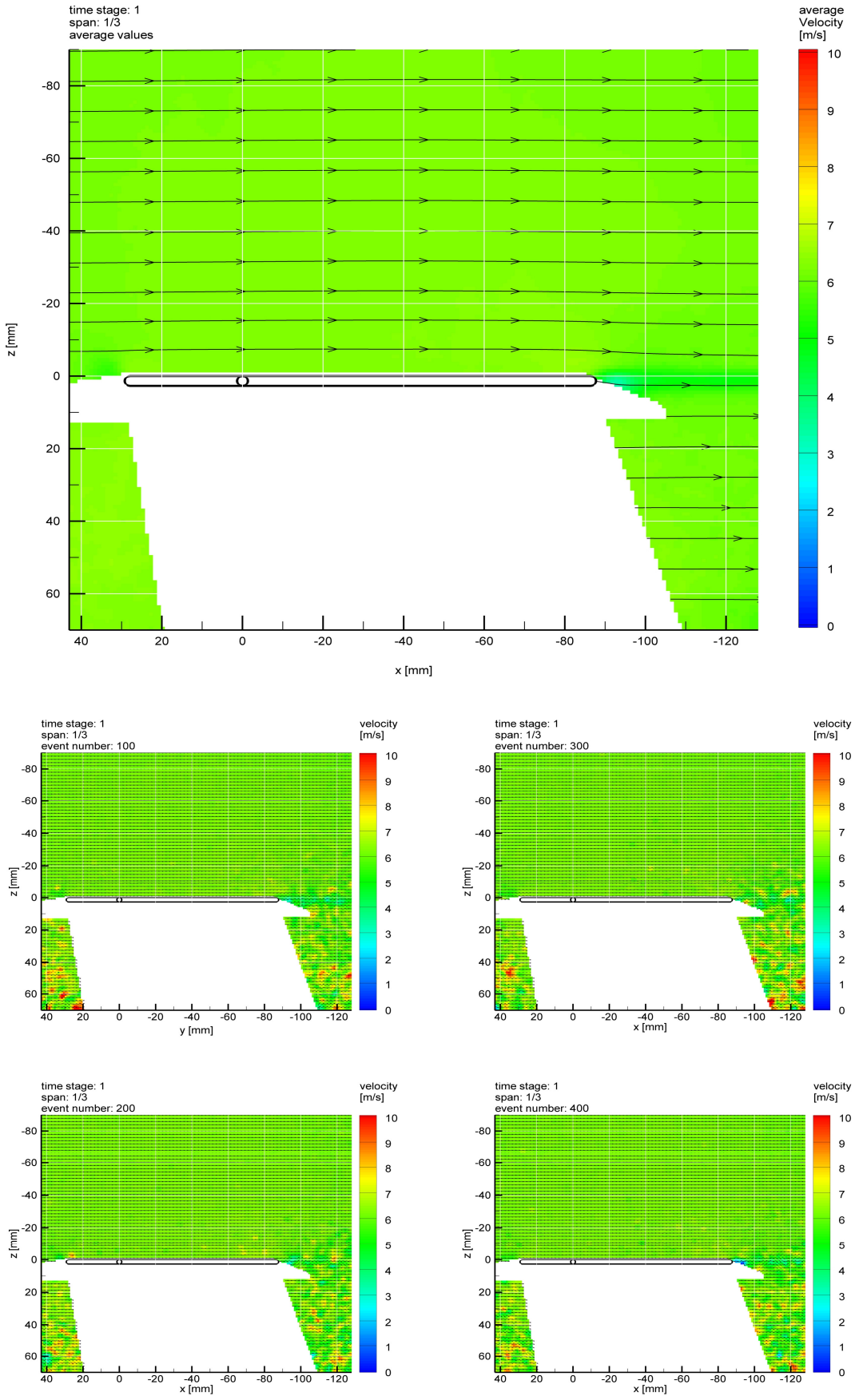

Figure 20: Velocity distributions for case I, time stage ① at 1/3 span

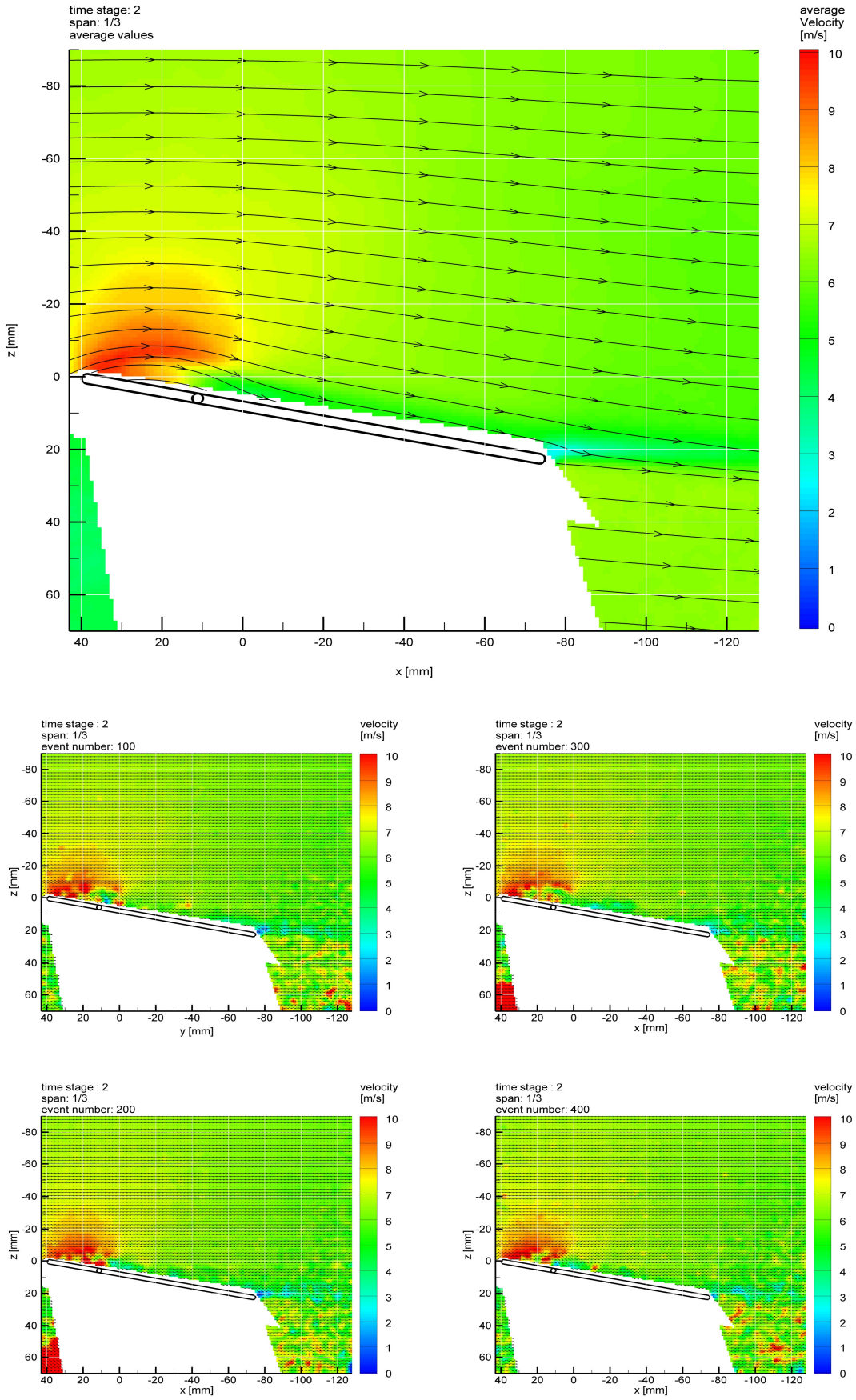

Figure 21: Velocity distributions for case I, time stage ② at 1/3 span

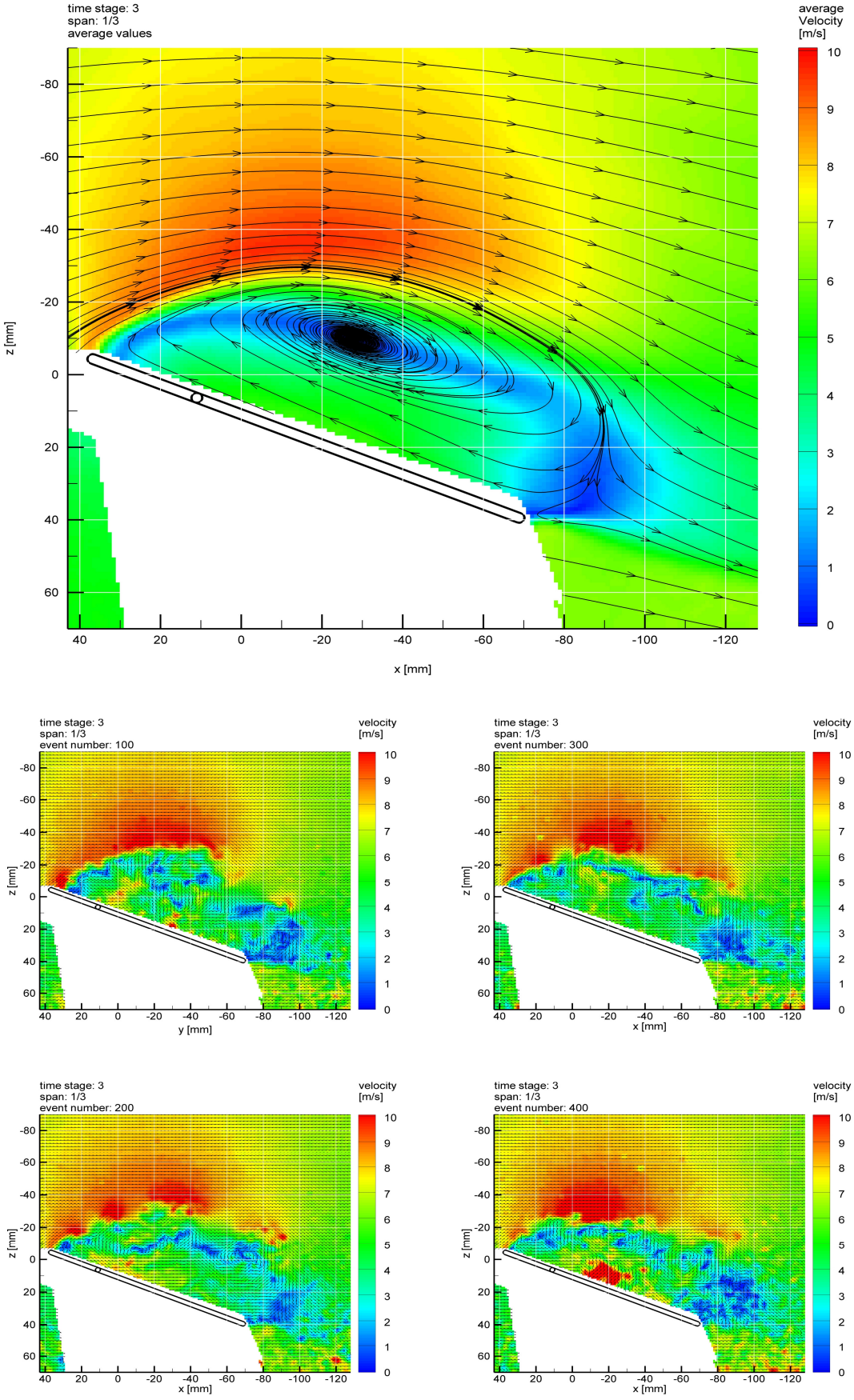

Figure 22: Velocity distributions for case I, time stage ③ at 1/3 span

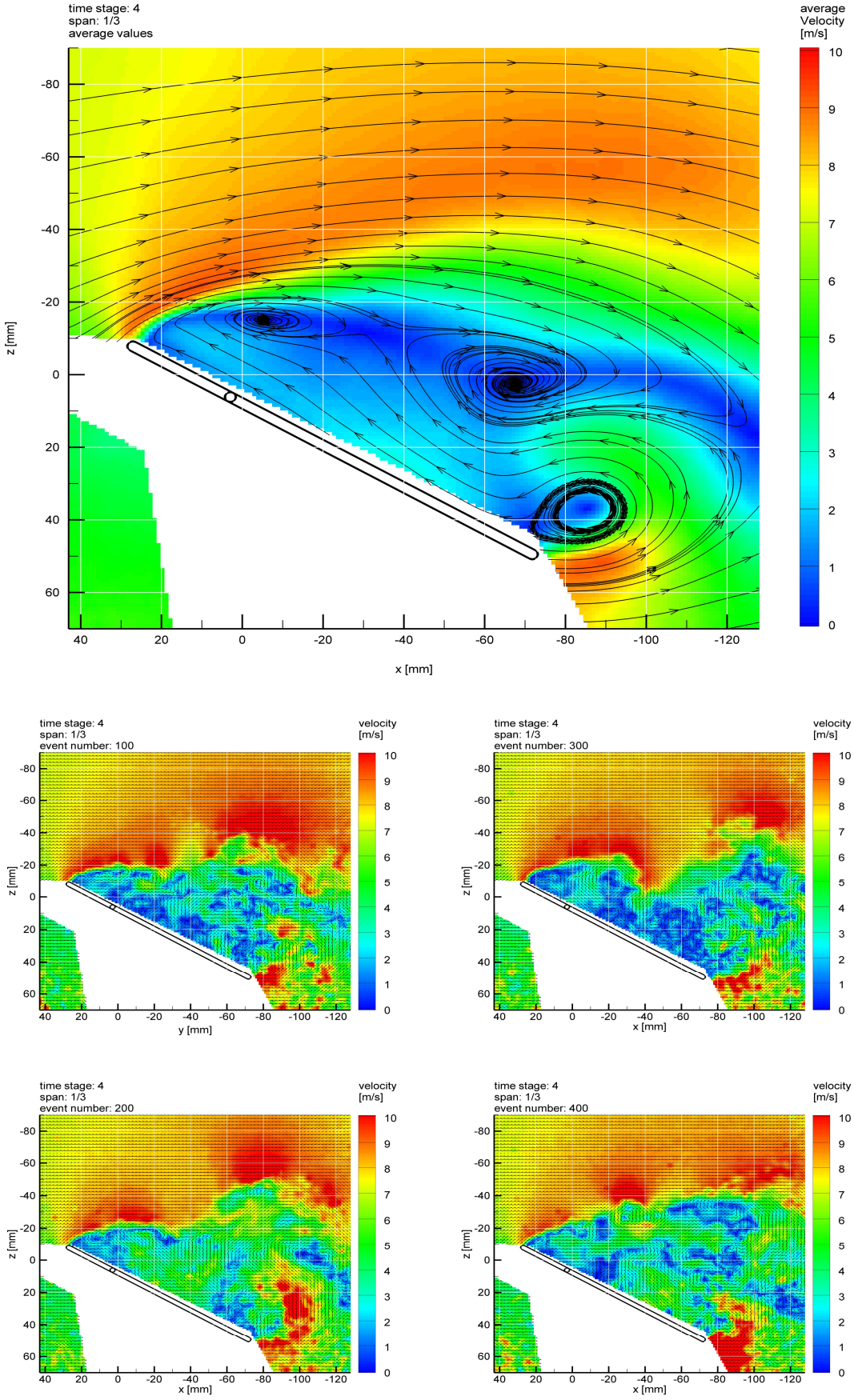

Figure 23: Velocity distributions for case I, time stage ④ at 1/3 span

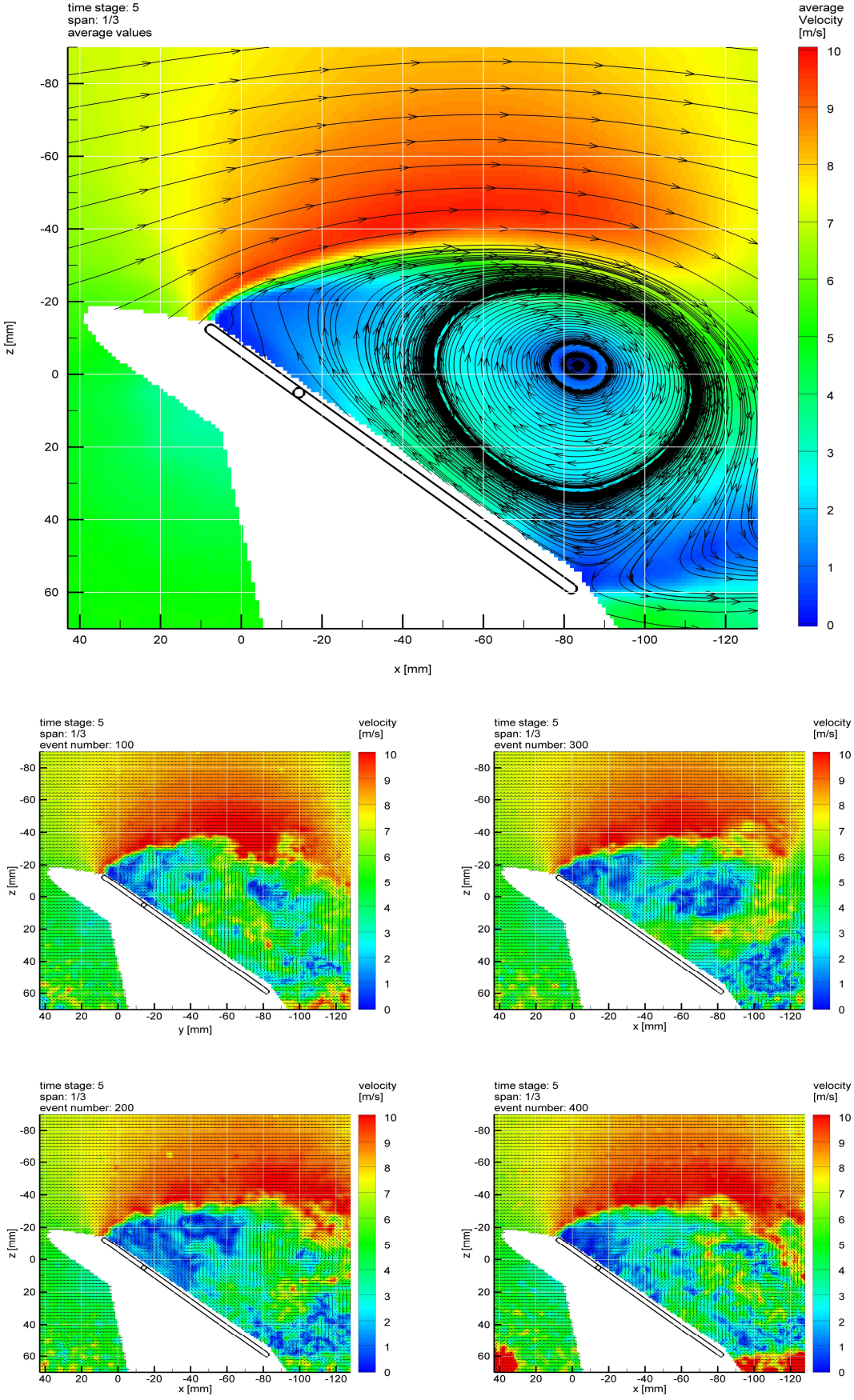

Figure 24: Velocity distributions for case I, time stage ⑤ at 1/3 span

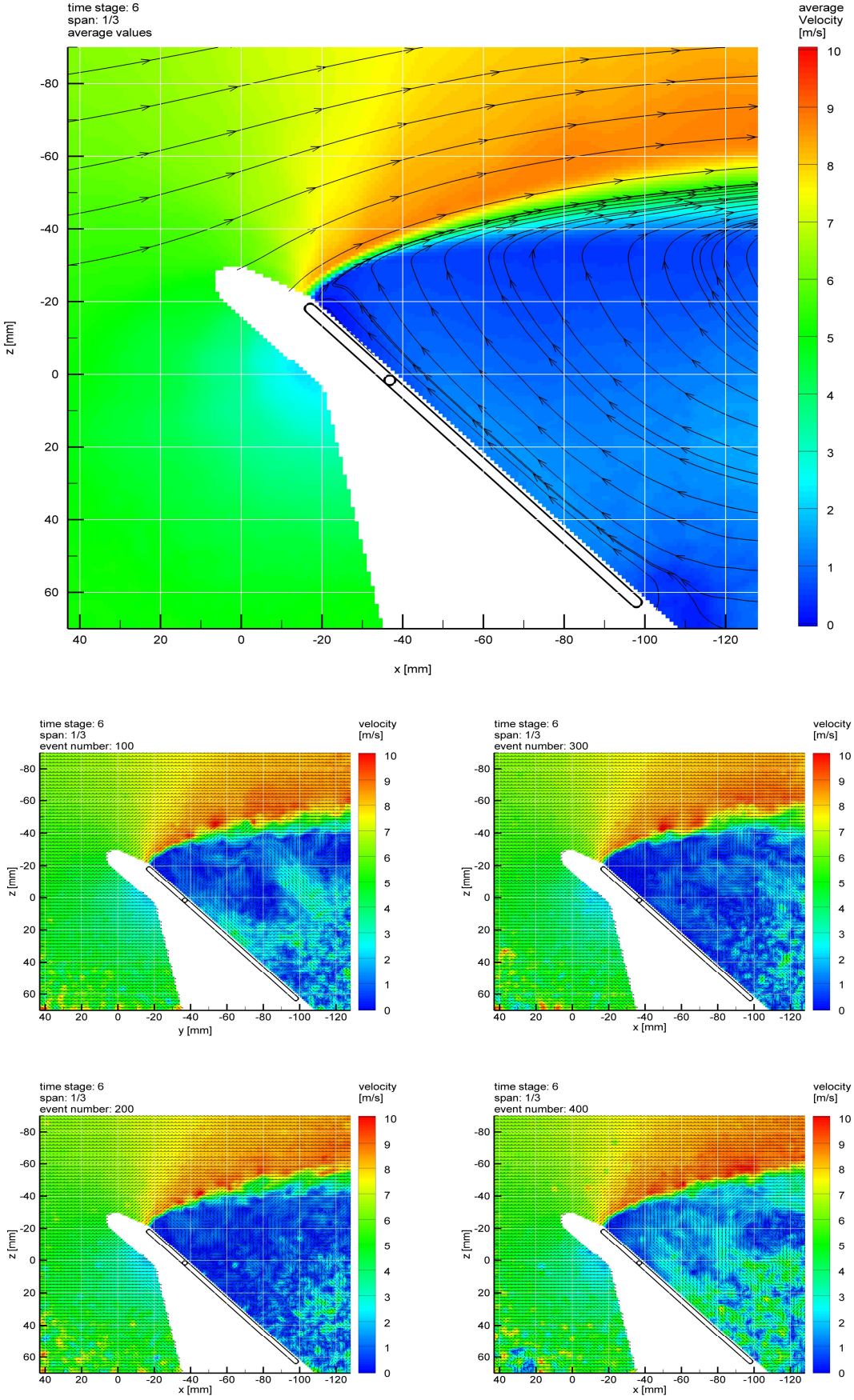

Figure 25: Velocity distributions for case I, time stage ⑥ at 1/3 span

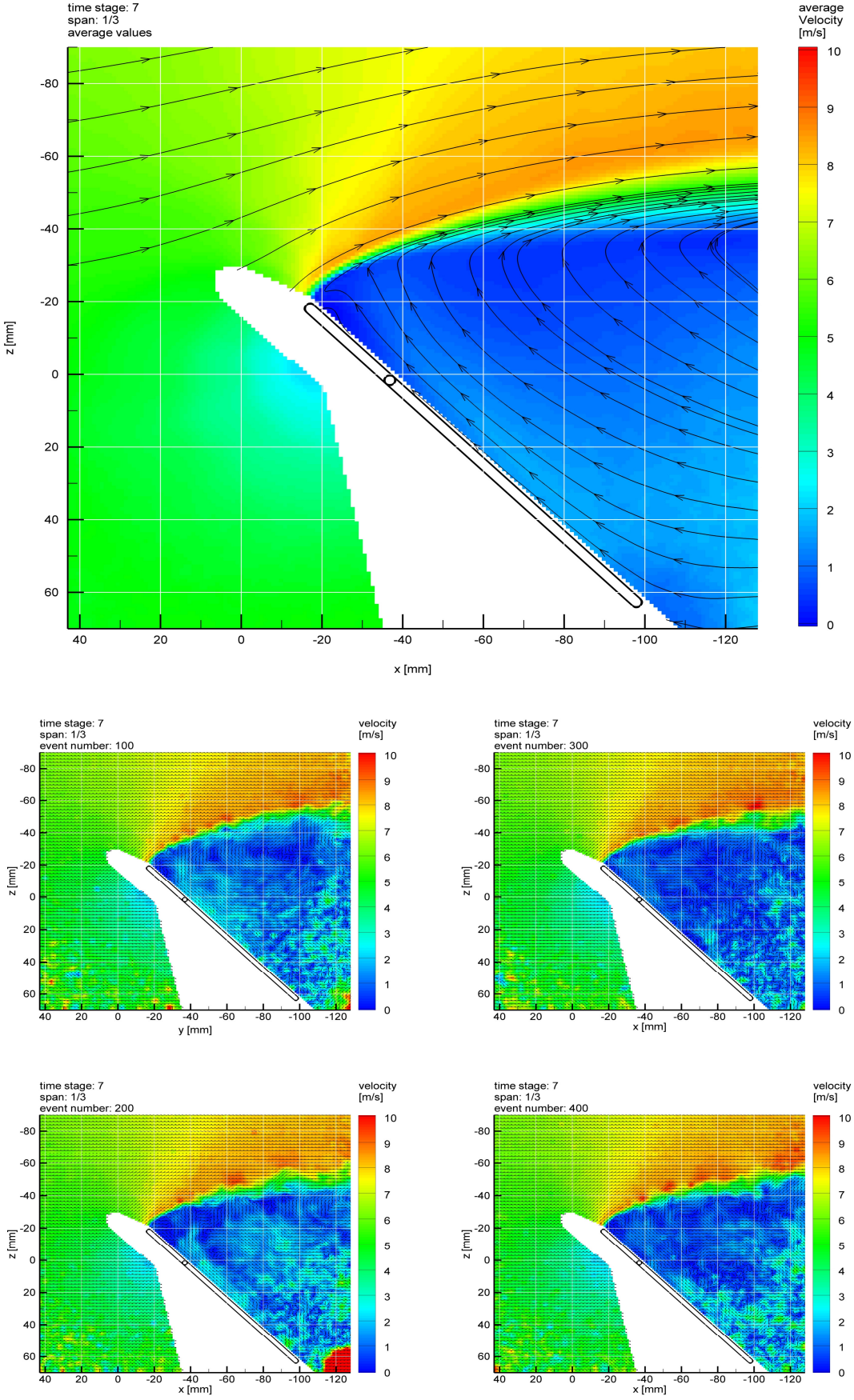

Figure 26: Velocity distributions for case I, time stage ⑦ at 1/3 span

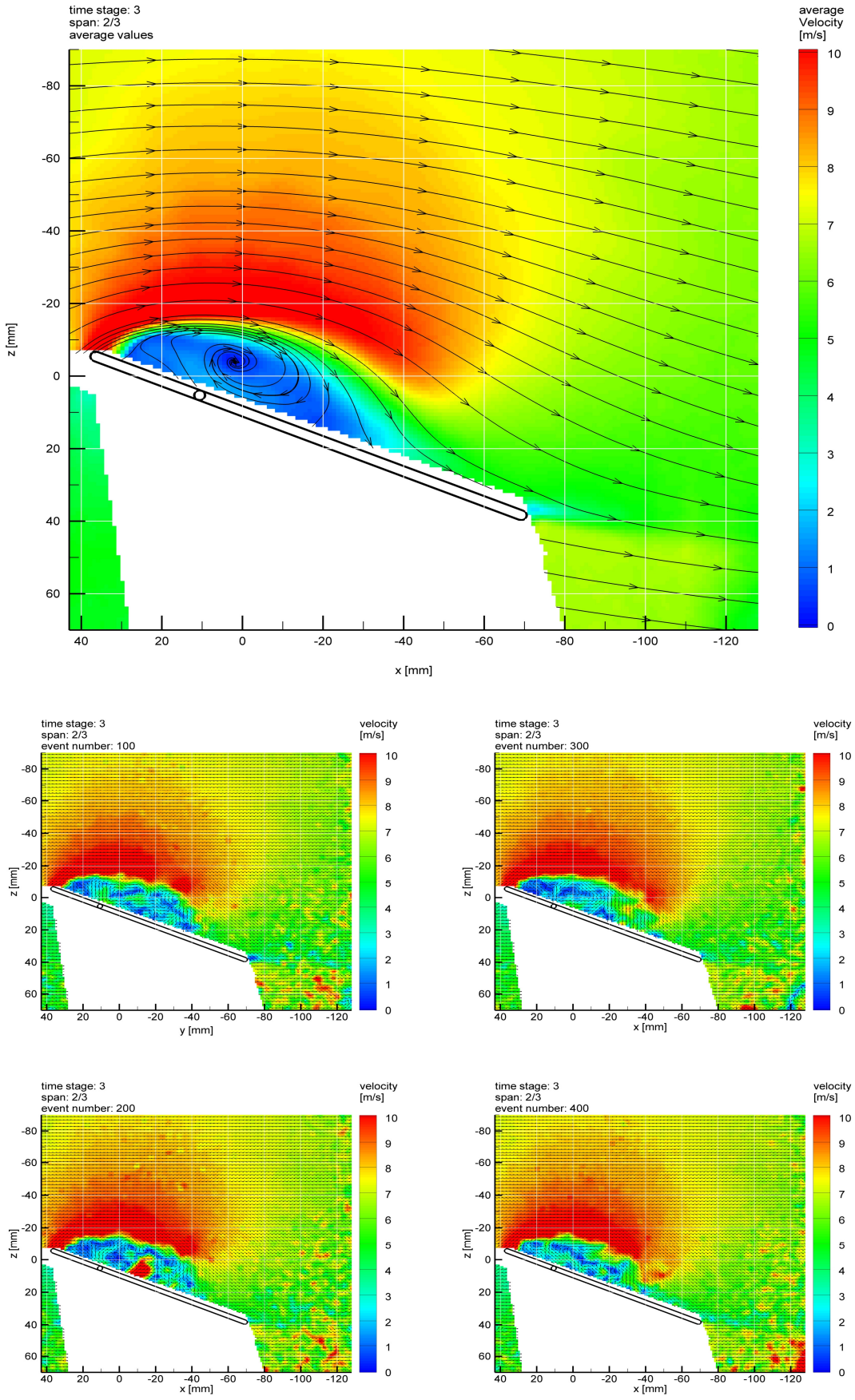

Figure 27: Velocity distributions for case I, time stage ③ at 2/3 span

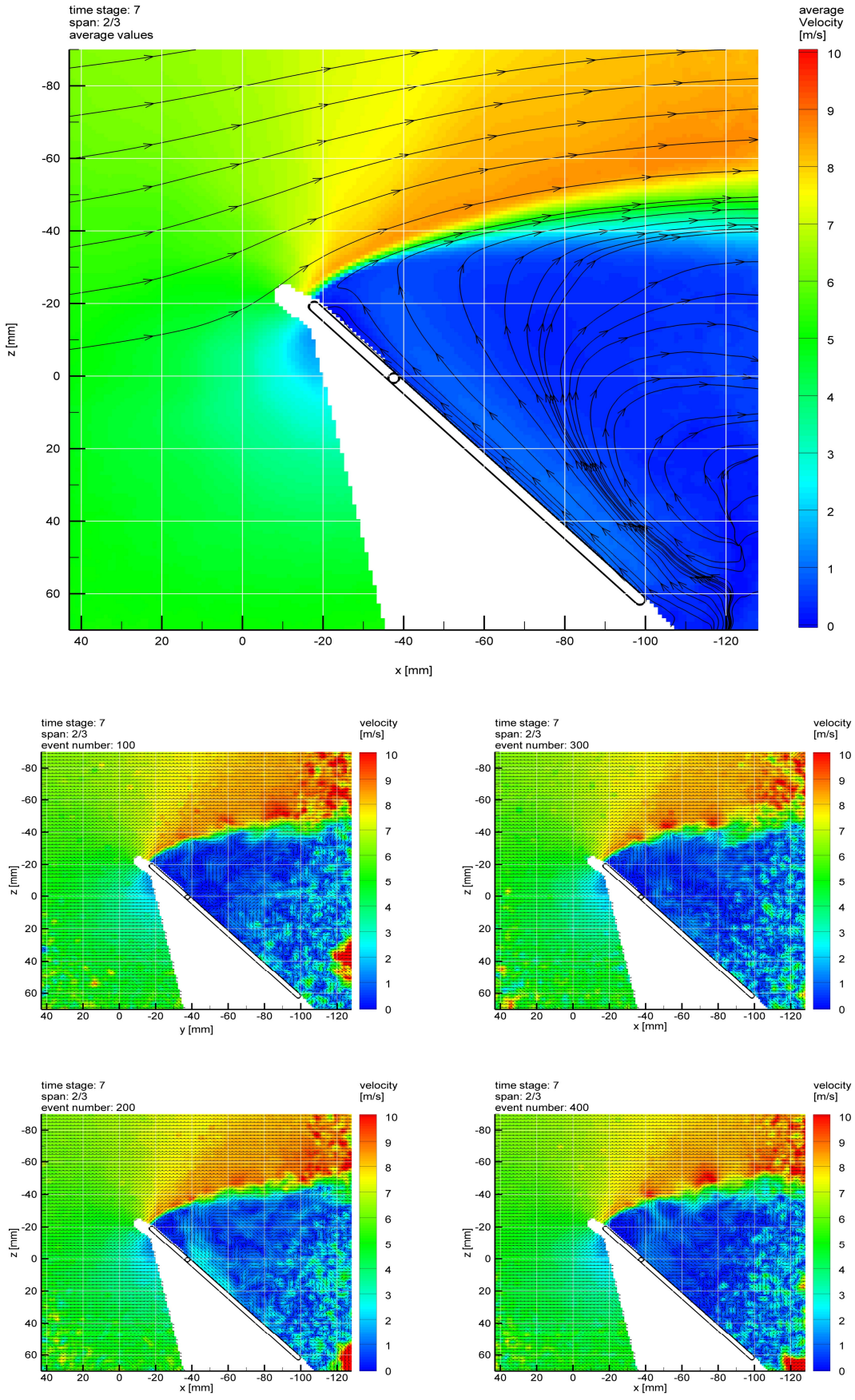

Figure 28: Velocity distributions for case I, time stage ⑦ at 2/3 span

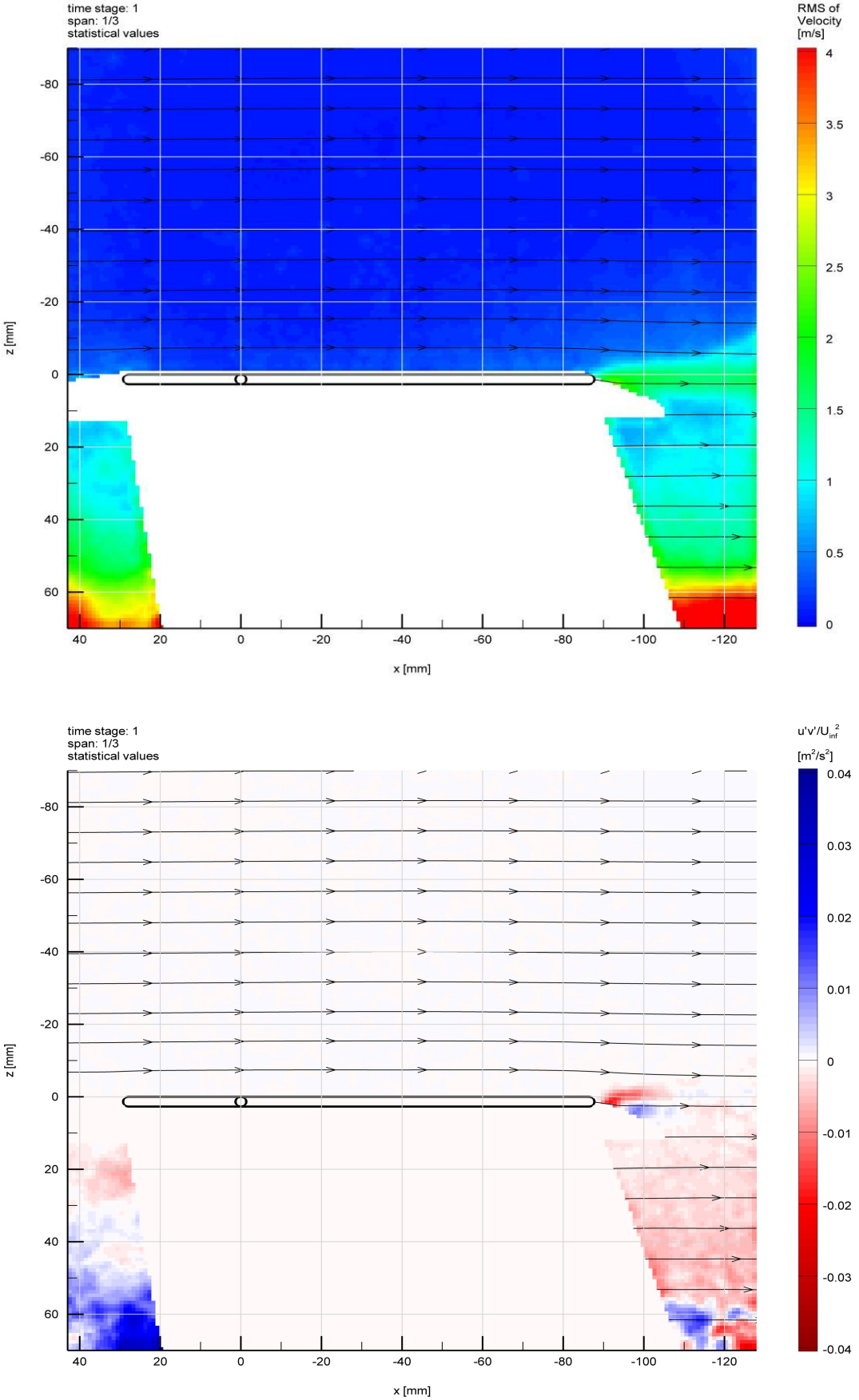

Figure 29: Statistical values excerpt for case I, time stage ① at 1/3 span: RMS of velocity and 2D-Reynolds stress component

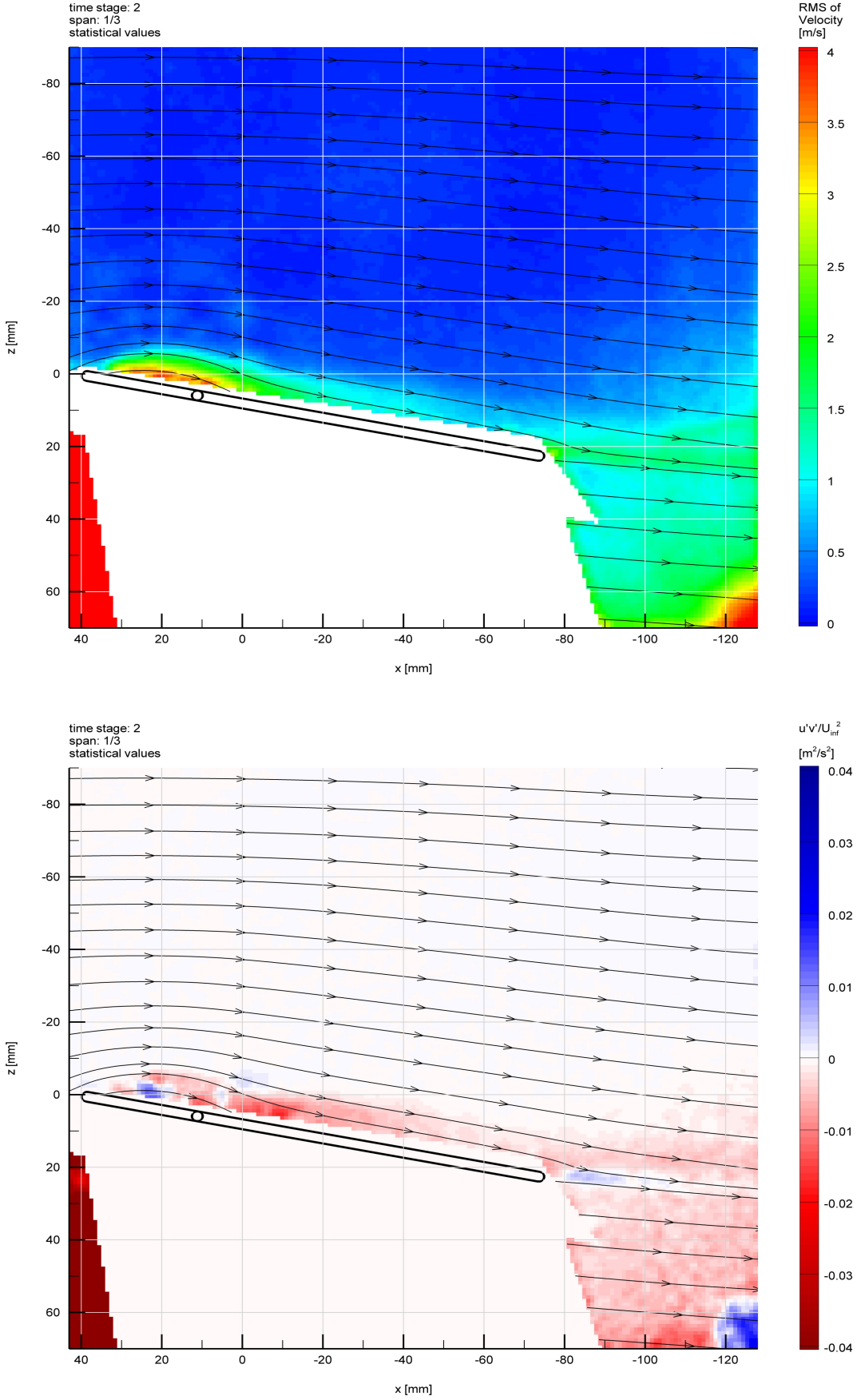

Figure 30: Statistical values excerpt for case I, time stage ② at 1/3 span: RMS of velocity and normalized 2D-Reynolds stress component u´v´

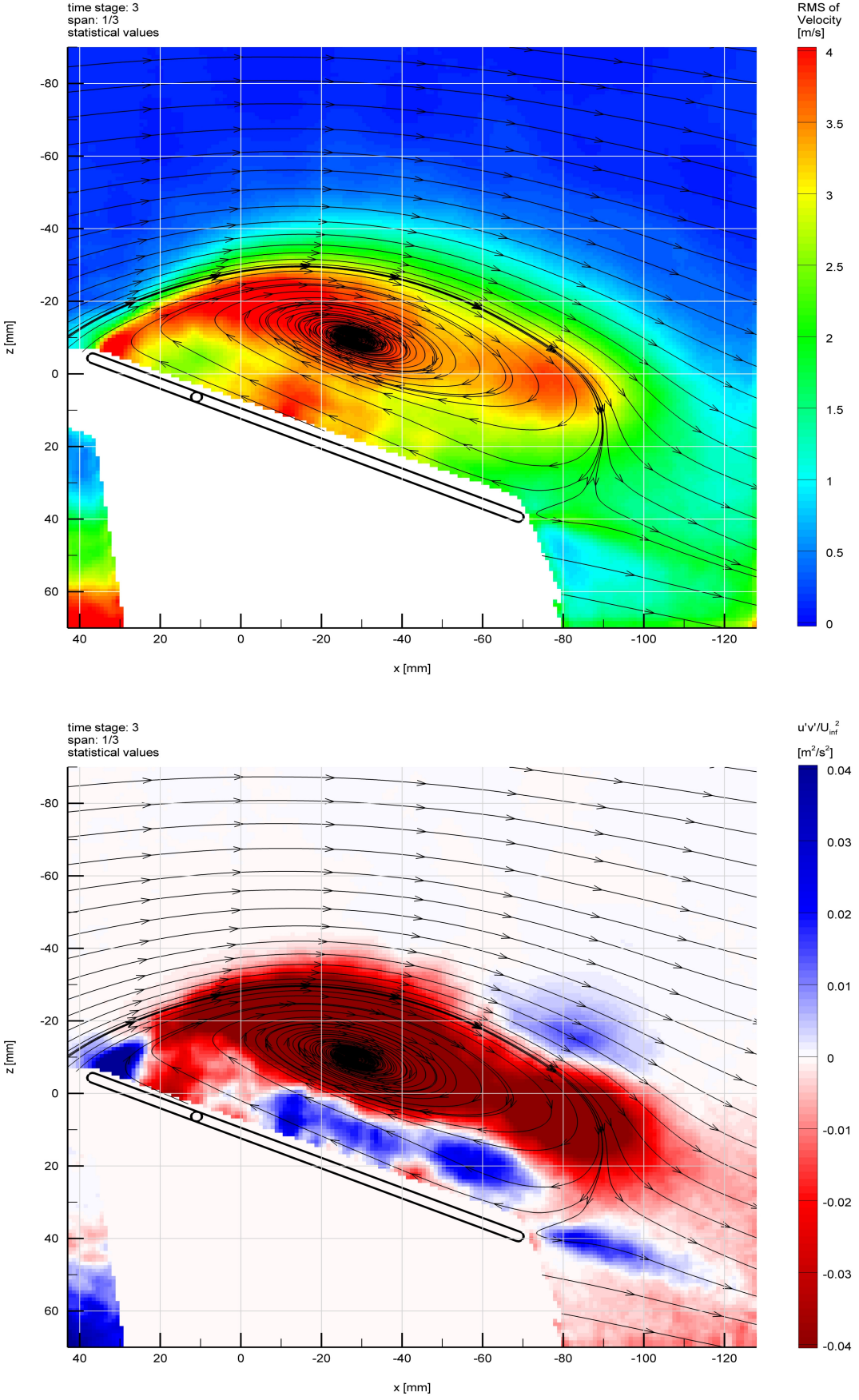

Figure 31: Statistical values excerpt for case I, time stage ③ at 1/3 span: RMS of velocity and normalized 2D-Reynolds stress component u´v´

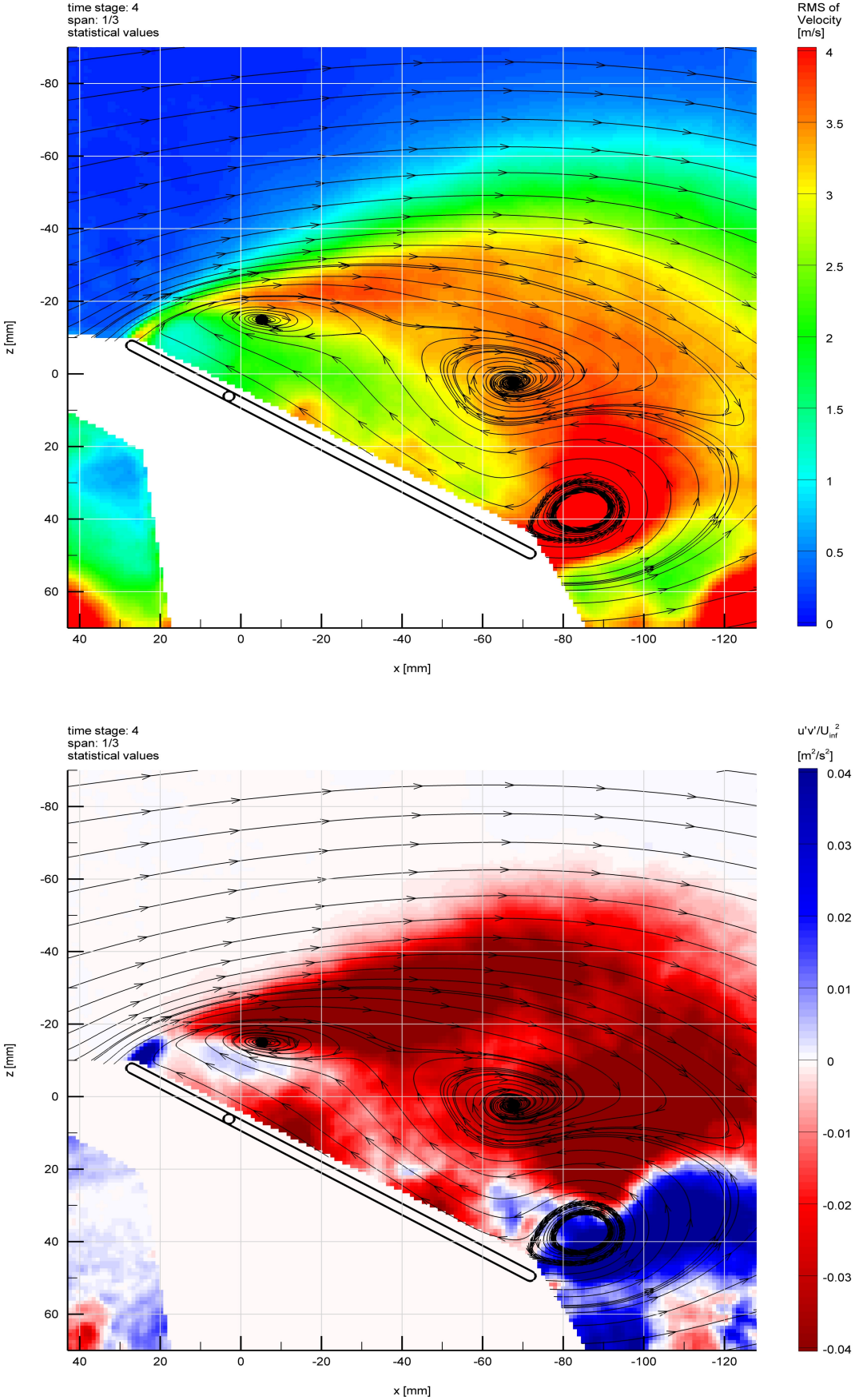

Figure 32: Statistical values excerpt for case I, time stage ④ at 1/3 span: RMS of velocity and normalized 2D-Reynolds stress component u´v´

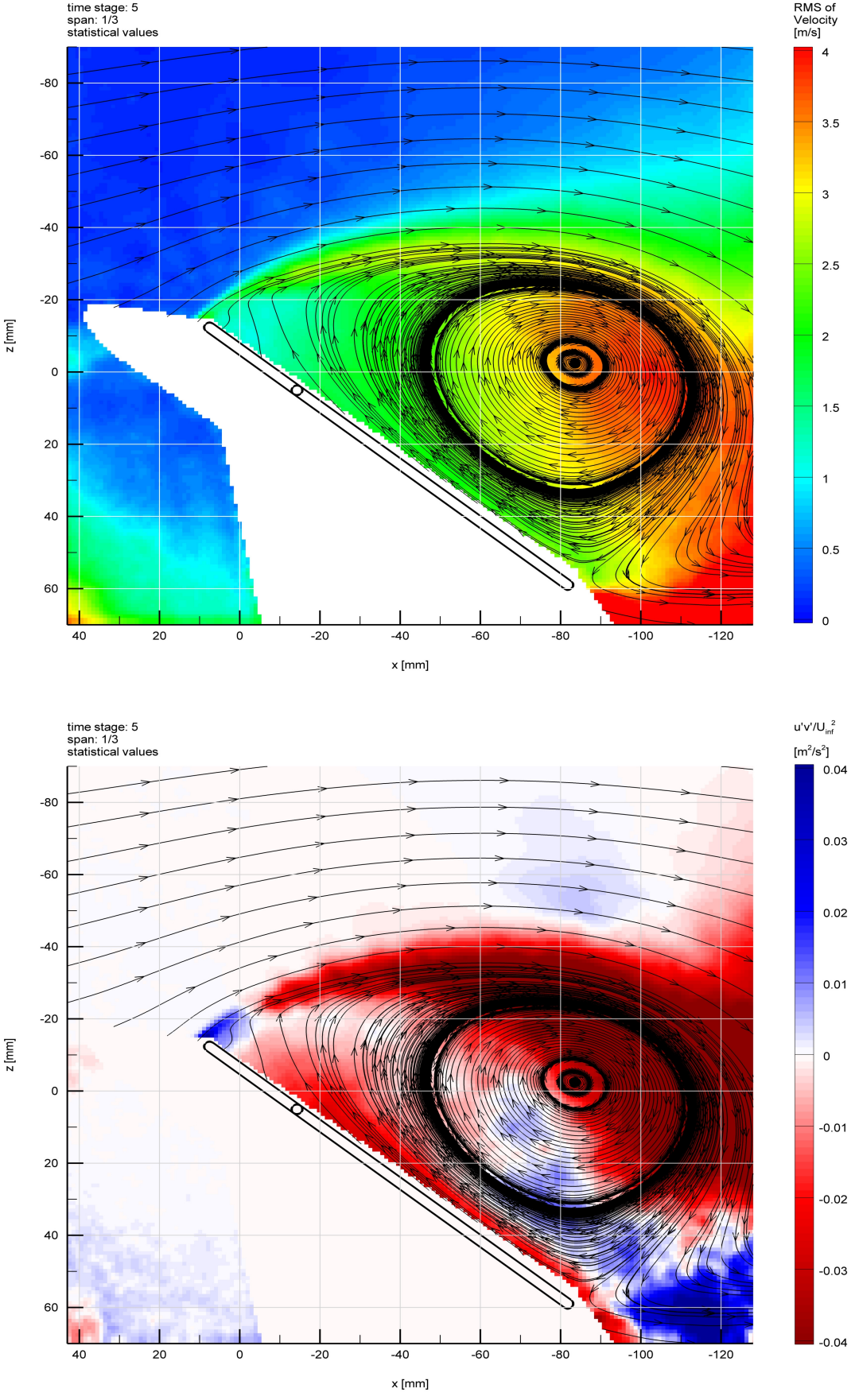

Figure 33: Statistical values excerpt for case I, time stage ⑤ at 1/3 span: RMS of velocity and normalized 2D-Reynolds stress component u´v´

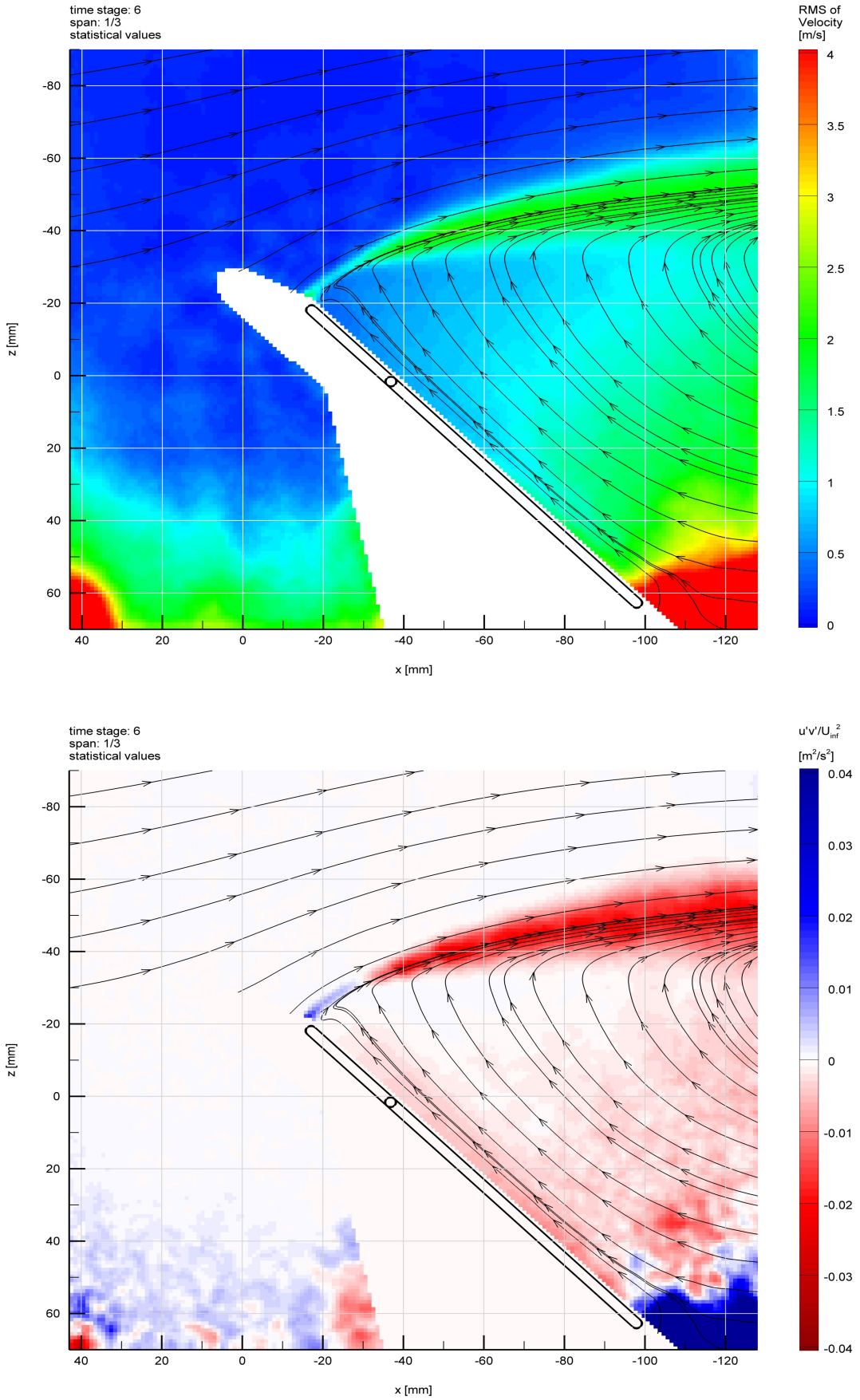

Figure 34: Statistical values excerpt for case I, time stage ⑥ at 1/3 span: RMS of velocity and normalized 2D-Reynolds stress component u´v´

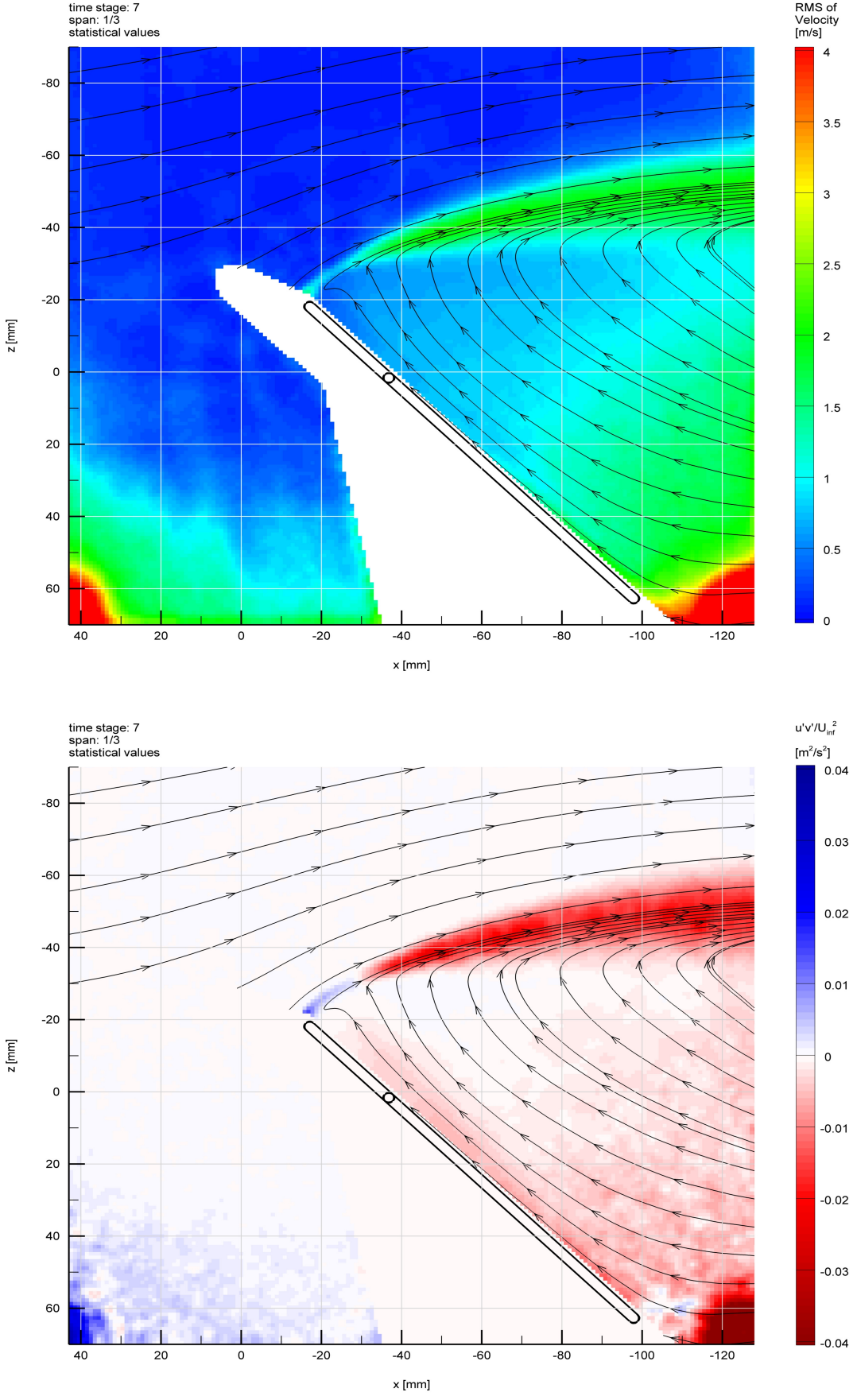

Figure 35: Statistical values excerpt for case I, time stage ⑦ at 1/3 span: RMS of velocity and normalized 2D-Reynolds stress component u´v´

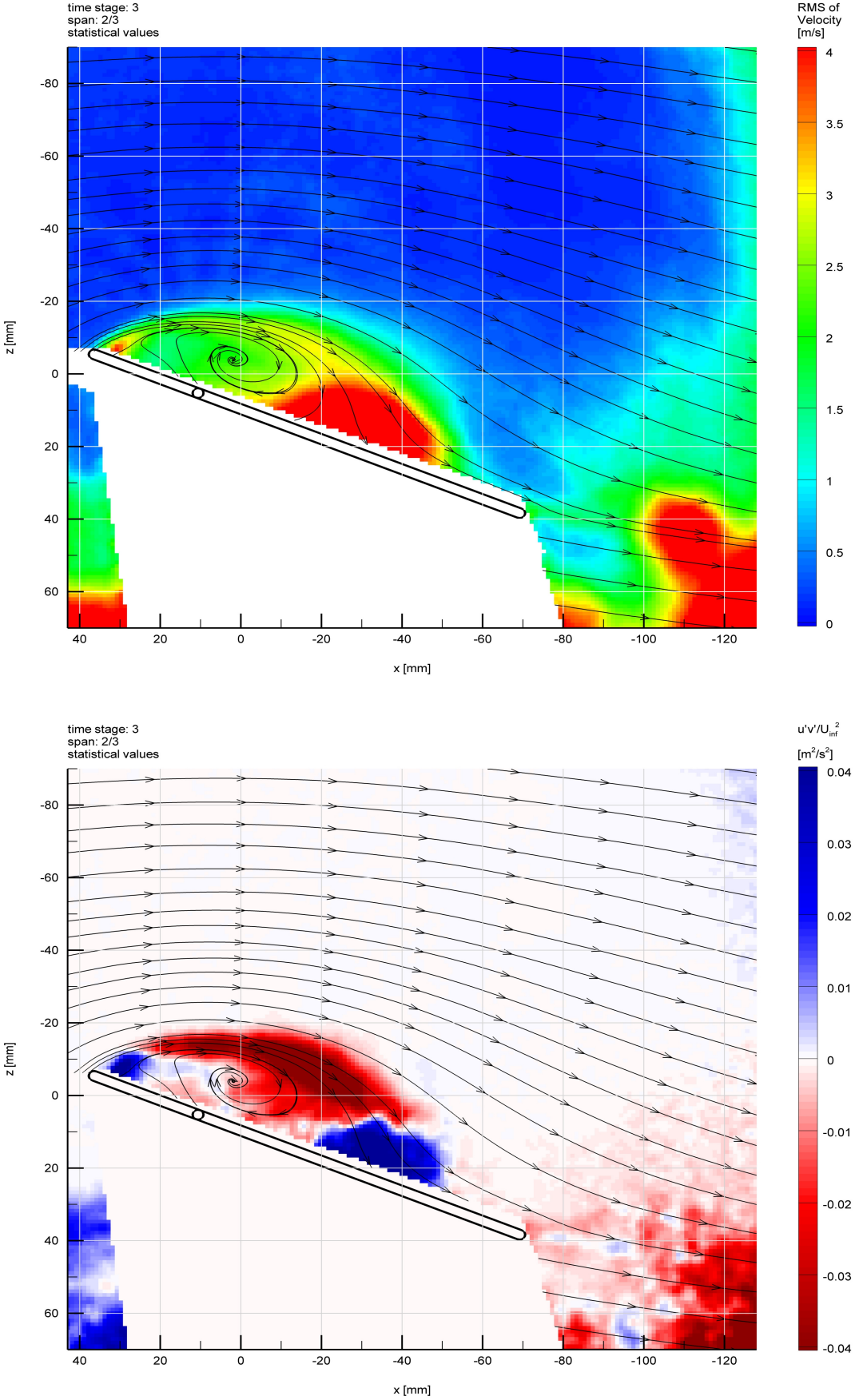

Figure 36: Statistical values excerpt for case I, time stage ③ at 2/3 span: RMS of velocity and normalized 2D-Reynolds stress component u´v´

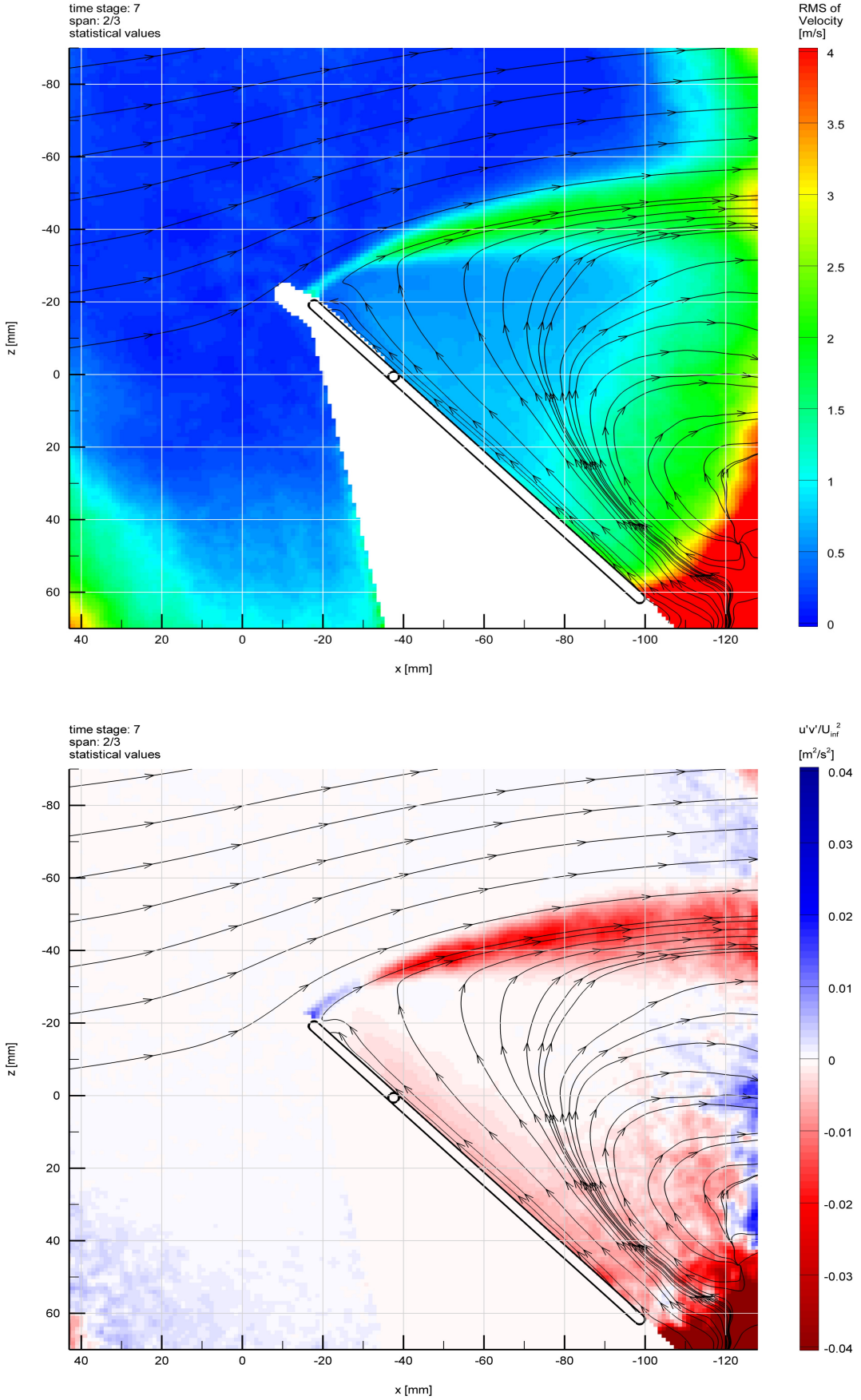

Figure 37: Statistical values excerpt for case I, time stage ⑦ at 2/3 span: RMS of velocity and normalized 2D-Reynolds stress component u´v´

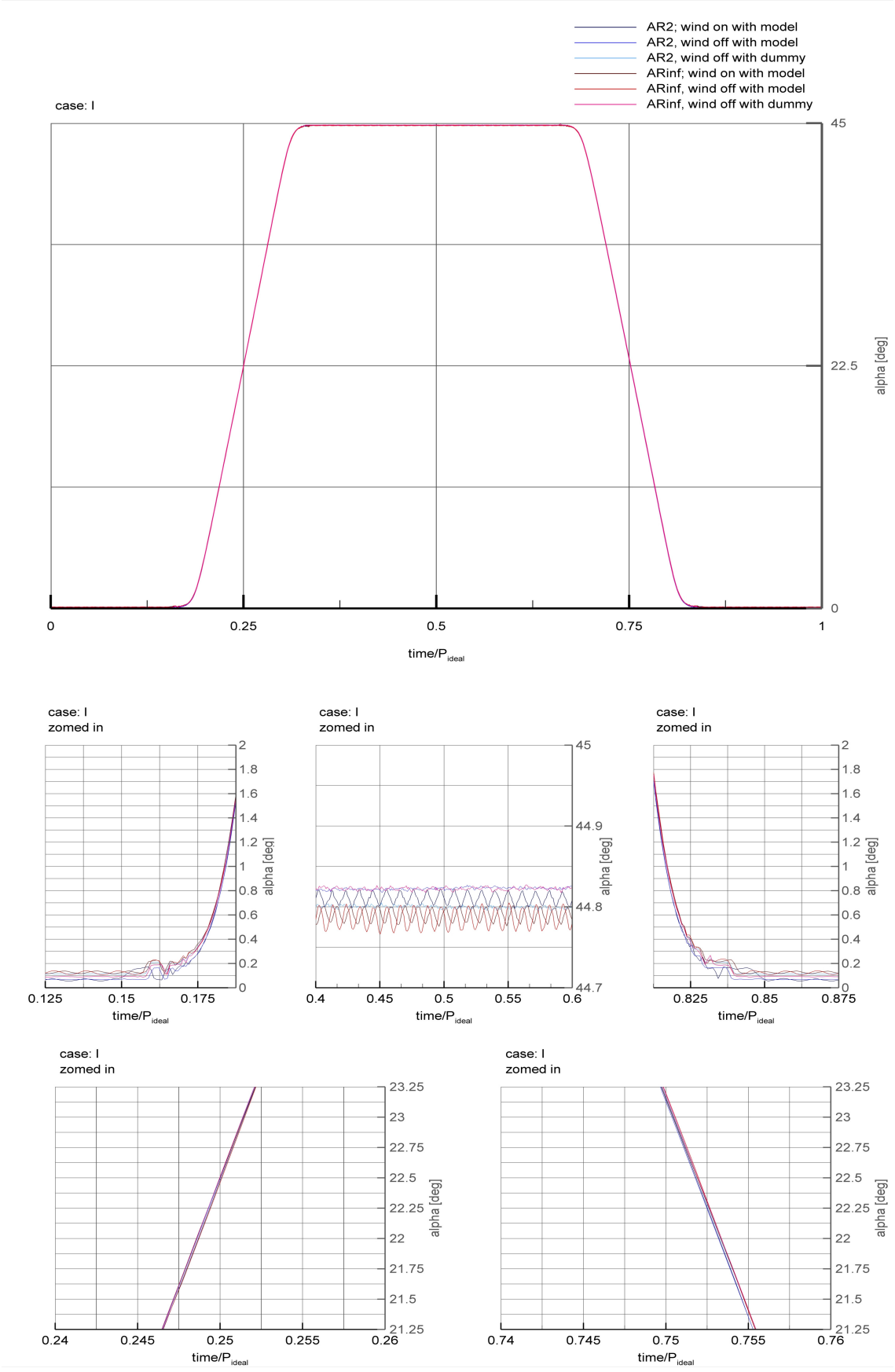

Figure 38: Position recordings of case I

B Stored Data

All recorded data (raw and processed by the mentioned software packages) including layouts of the plots made with *tecplot 360 2009*, together with a copy of this report are stored on an external hard disc for further access. The order of the stored folders and the filenames are self-explanatory.

Addendum

The following contains the results of the repeated force measurements in October 2010 after the balance had been repaired and checked. With the chordwise force measured, the forces can be transformed into the aerodynamic coordinate system.
The figures 39 to 48 show the aerodynamic coefficients of the first and second measurement in side to side comparison. It can be seen, that both normal force and pitching moment were measured correctly in the first run already (except for the fact, that the pitching moment had a wrong sign). The differences are partially based on the influence of the wrongly measured components of the damaged balance through the component composition matrixes of the balance and partially show the repeat accuracy between two such measurement campaigns.
The chordwise force component turns out to be so small, that it is almost lost inside measurement noise and calibration error. Thus, it cannot contribute substantially during the transformation into lift and drag.
The lift slopes – as a consequence of the coordinate system transformation - show a larger distance between the peak values and the quasi-static level. For the same reason the following multiple peaks are not so easily detected in the lift and drag slopes as in the normal force and pitching moment slopes.

Since the second measurement verifies the first but gives no more insight, the analysis in the above report does not need any modification.

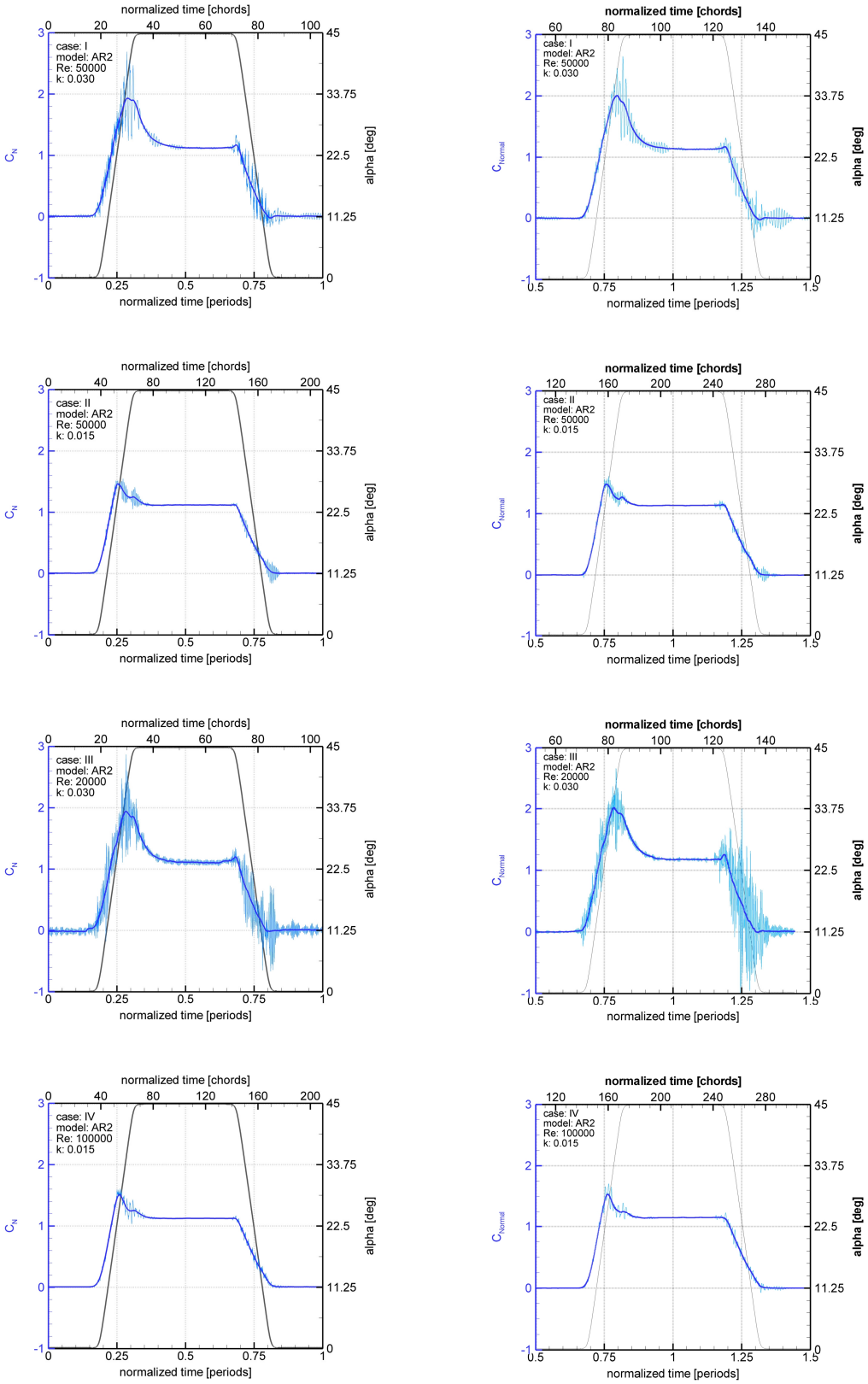

Figure 39: Normal force measurements of the *AR2* model
before (left) and after (right) the balance repair.
(Low pass Bessel filter frequencies: 200Hz and 25Hz)

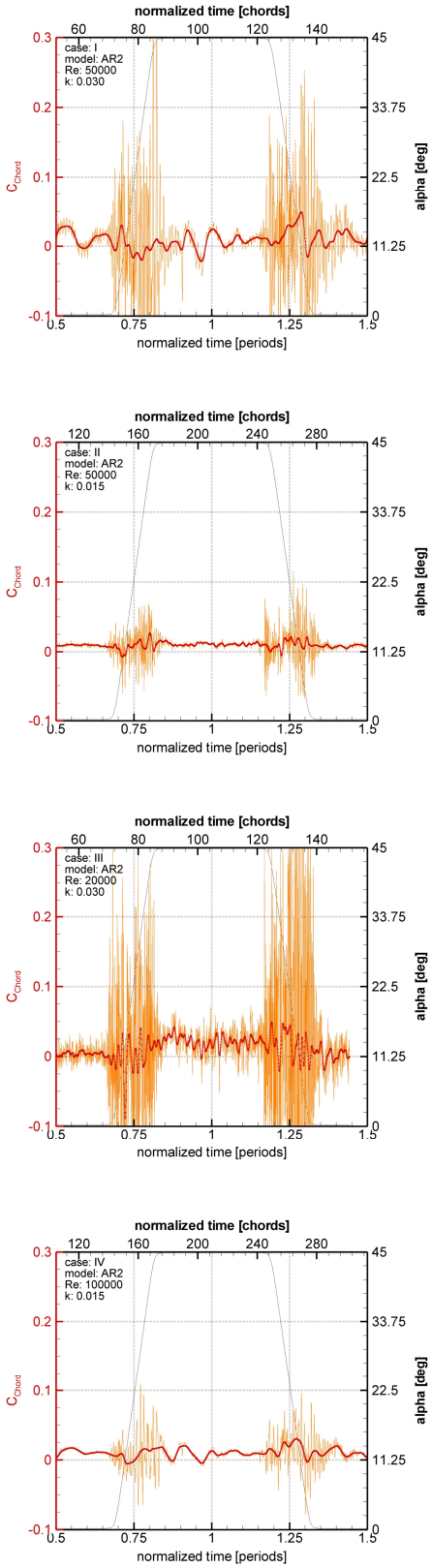

Figure 40: Chordwise force measurements of the *AR2* model after the balance repair.
(Low pass Bessel filter frequencies: 200Hz and 25Hz)

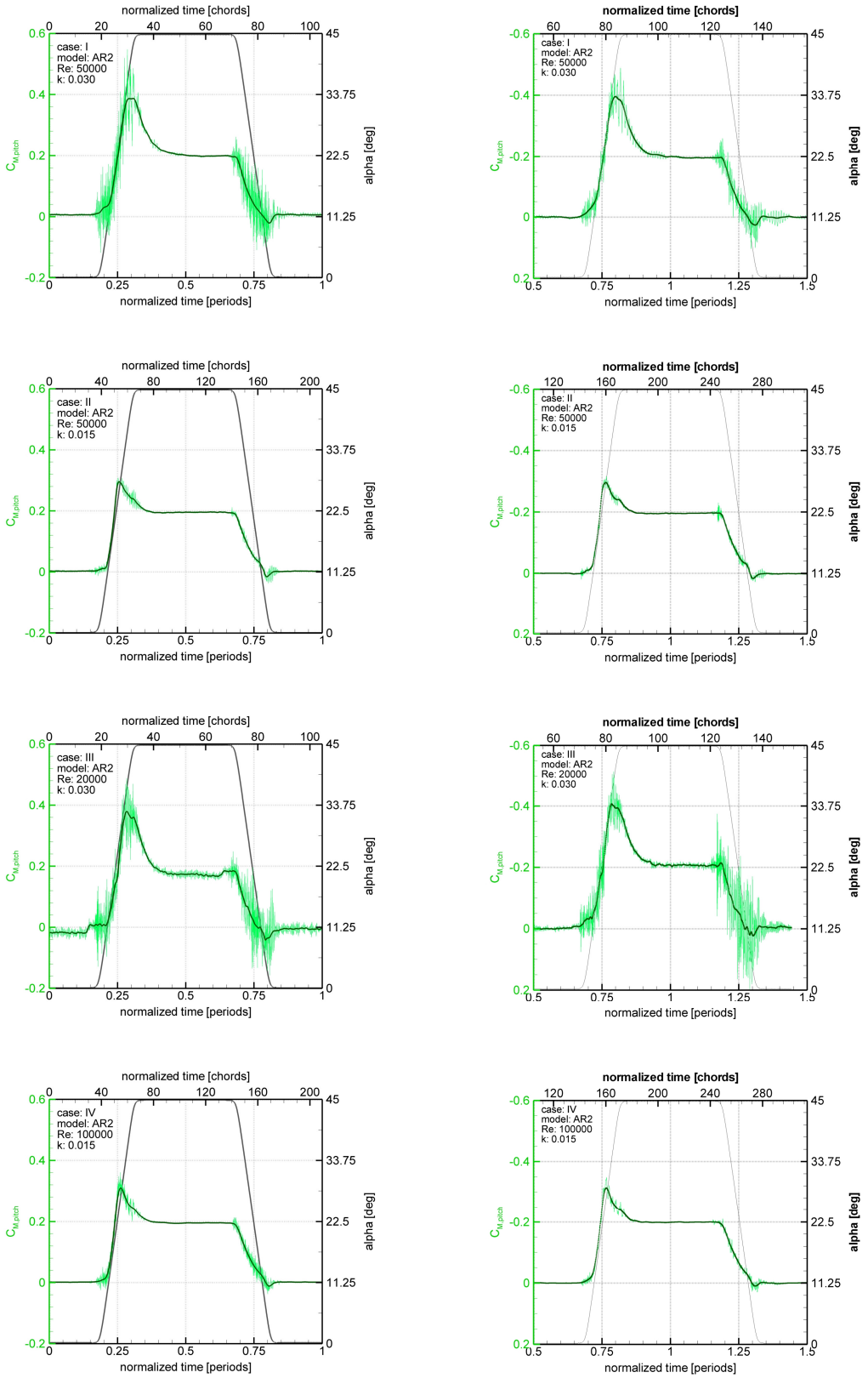

Figure 41: Pitching moment measurements of the *AR2* model before (left) and after (right) the balance repair. (Low pass Bessel filter frequencies: 200Hz and 25Hz)

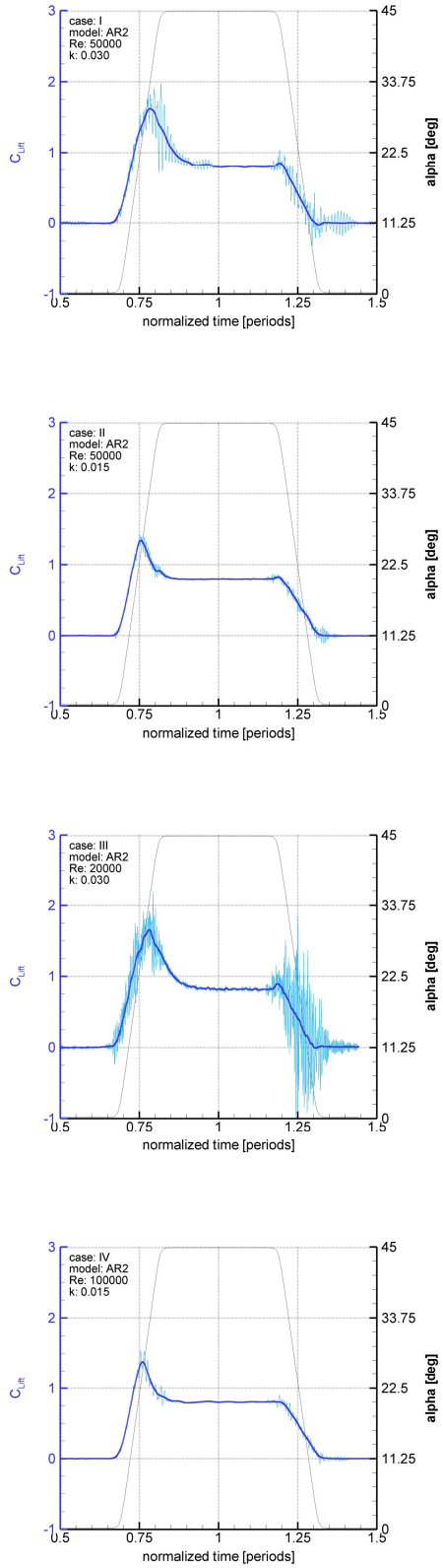

Figure 42: Lift measurements of the *AR2* model
after the balance repair.
(Low pass Bessel filter frequencies: 200Hz and 25Hz)

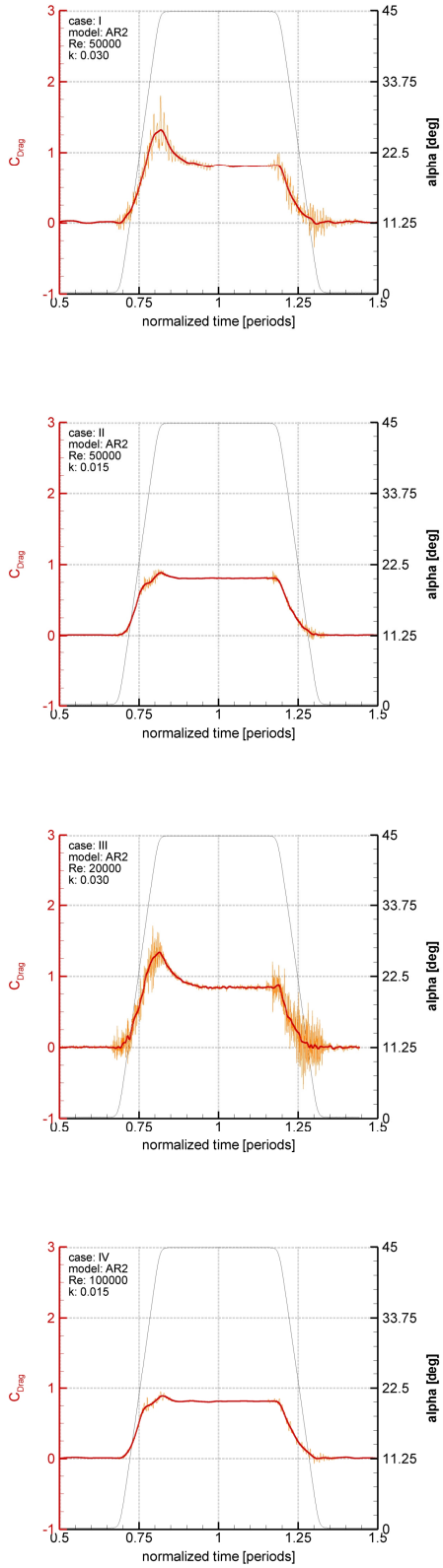

Figure 43: Drag measurements of the *AR2* model
after the balance repair.
(Low pass Bessel filter frequencies: 200Hz and 25Hz)

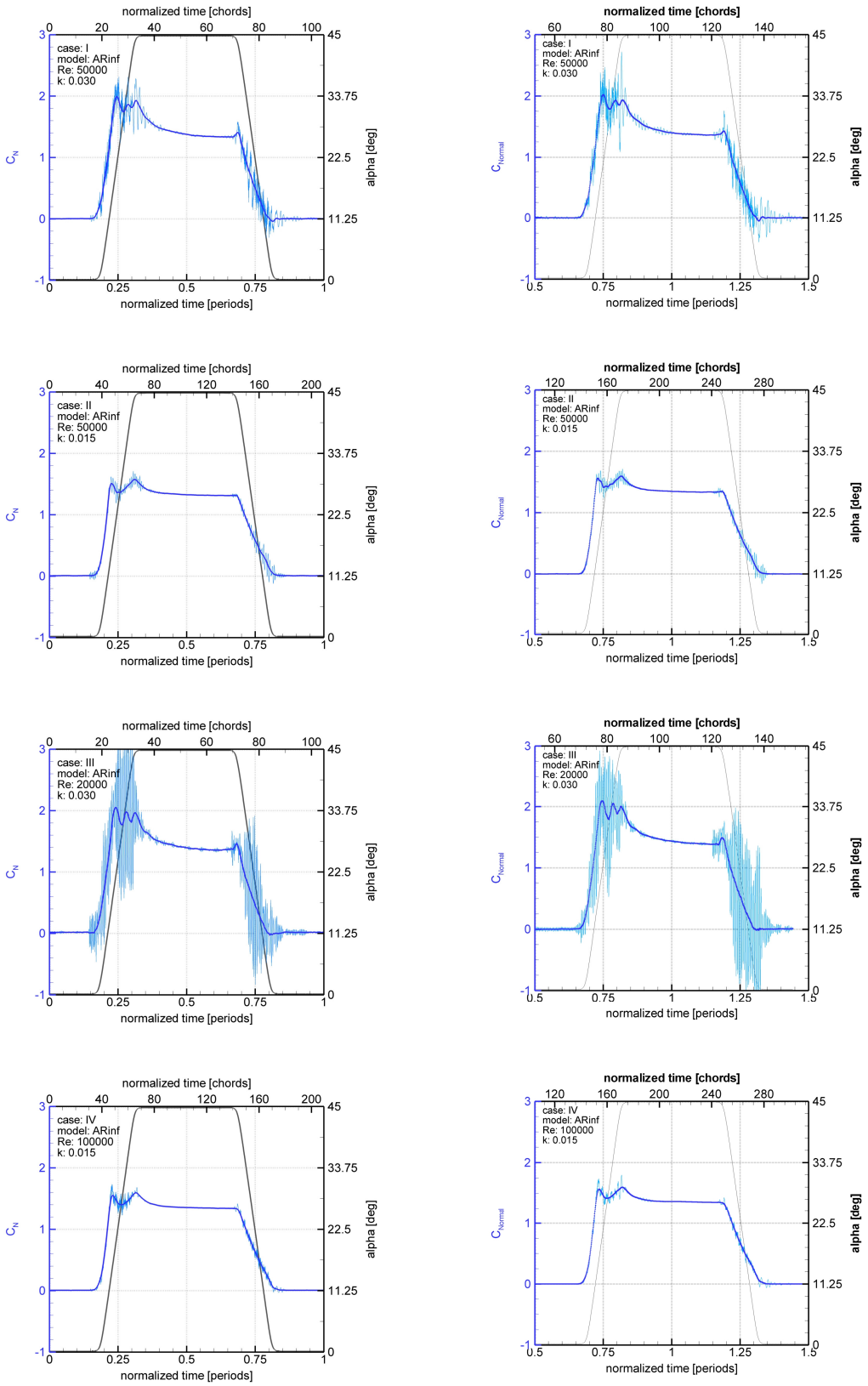

Figure 44: Normal force measurements of the *ARinf* model before (left) and after (right) the balance repair. (Low pass Bessel filter frequencies: 200Hz and 25Hz)

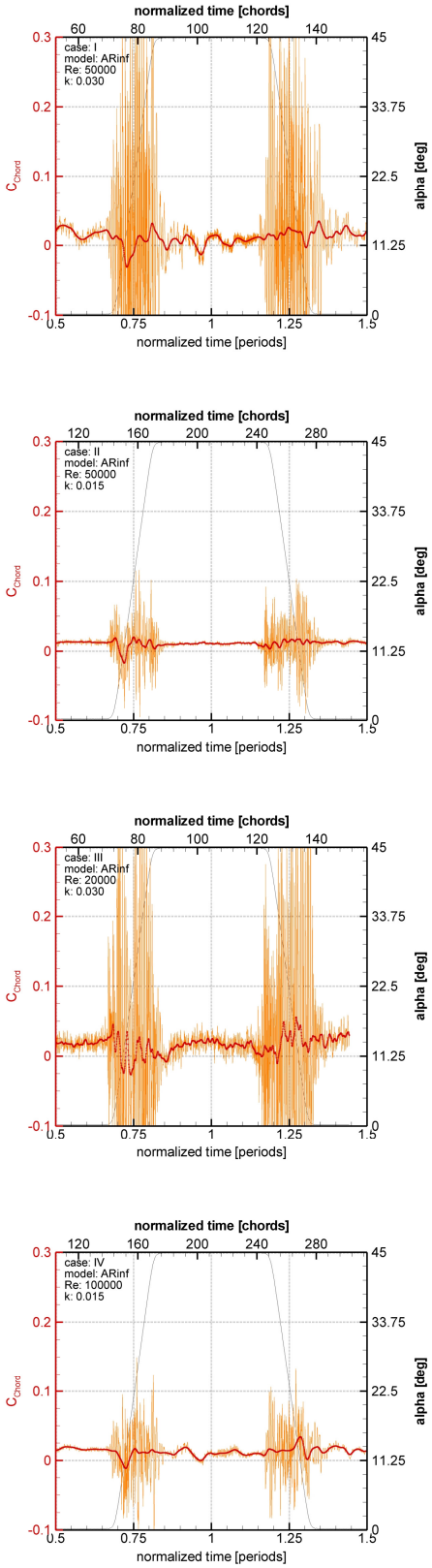

Figure 45: Chordwise force measurements of the *ARinf* model after the balance repair.
(Low pass Bessel filter frequencies: 200Hz and 25Hz)

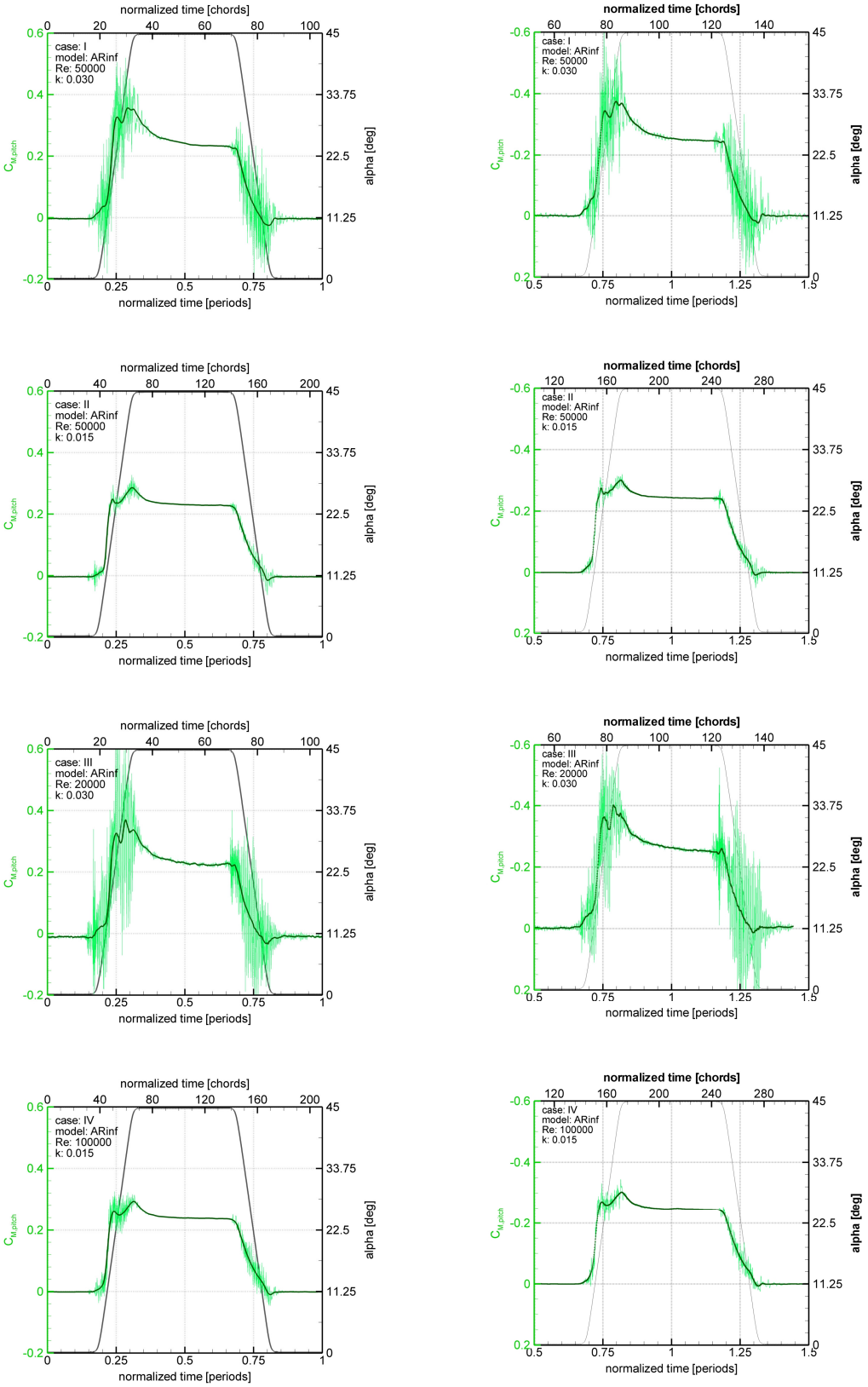

Figure 46: Pitching moment measurements of the *ARinf* model before (left) and after (right) the balance repair. (Low pass Bessel filter frequencies: 200Hz and 25Hz)

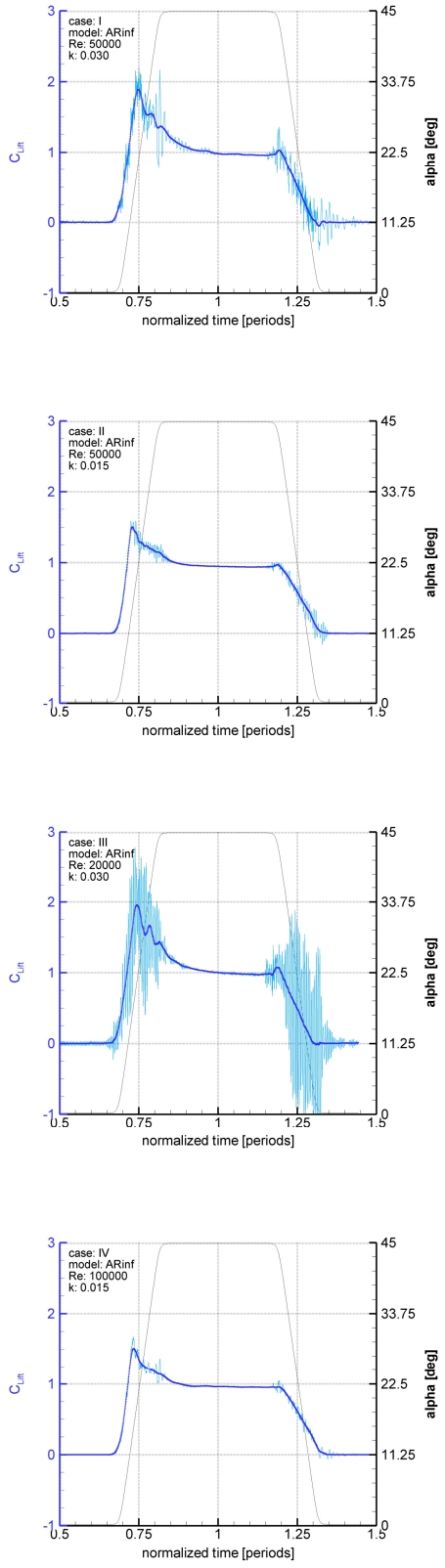

Figure 47: Lift measurements of the *ARinf* model
after the balance repair.
(Low pass Bessel filter frequencies: 200Hz and 25Hz)

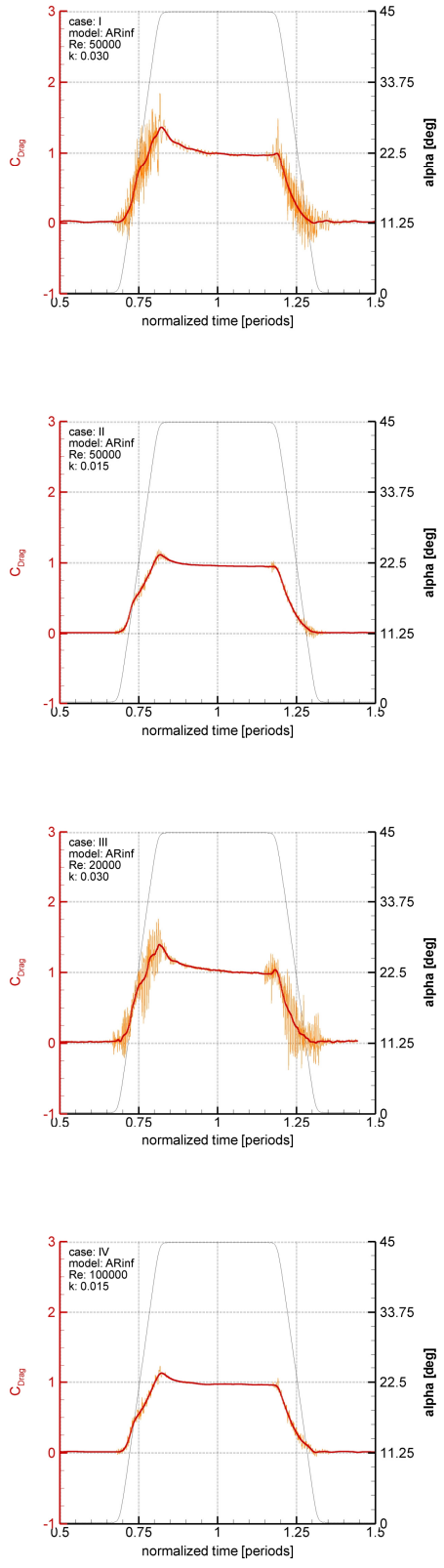

Figure 48: Drag measurements of the *ARinf* model
after the balance repair.
(Low pass Bessel filter frequencies: 200Hz and 25Hz)